Dry Metal Forming Open Access Journal

Final Project Report

Edited by Frank Vollertsen
Available online at https://elib.suub.uni-bremen.de

www.drymetalforming.de

Dry Met. Forming OAJ FPR 6 (2020) 262–301
Date of Report 16 April 2020; published 12 Juni 2020

Dry deep drawing of aluminum for automotive production

(DFG Grant No. VO 530/75; SCHU 1484/16; MU 3093/2, Funding Period 01.01.2014 – 31.03.2018)

Markus Prieske*[1], Richard Börner*[3], Thomas Berger[3], Ralf Kühn[3], Peter Scholz*[4], Andreas Schubert[3], Roland Müller[4], Frank Vollertsen[1,2]

[1]BIAS – Bremer Institut für angewandte Strahltechnik GmbH, Klagenfurter Str. 5, 28359 Bremen, Germany
[2]University of Bremen, Bibliothekstr. 1, 28359 Bremen, Germany
[3]MFT – Professur Mikrofertigungstechnik, TU Chemnitz, Reichenhainer Straße 70, 09126 Chemnitz, Germany
[4]IWU – Fraunhofer-Institut für Werkzeugmaschinen und Umformtechnik IWU, Reichenhainer Strasse 88, 09126 Chemnitz, Germany

Summary

Lubricants are commonly used in metal forming processes to reduce the friction between the workpiece and the forming tool to protect semi-finished products and goods against corrosion and to reduce the load on the tool. One aim of environmentally friendly production technologies is to achieve dry forming without the use of lubricants. The goal of this project is to enable the dry forming of aluminum alloys during deep drawing by locally increasing the tool load capacity using customized tool coatings. The suitability of two types of carbon-based coatings, amorphous carbon and CVD diamond coatings will be investigated for dry contact with aluminum. In addition to coating, tribological effective microstructuring should improve the material flow and wear resistance of the used tools. The advantage of the amorphous carbon coatings is the deposition process, which enables a large area deposition as well as a good adhesion strength on steel substrates. Dry strip drawing and deep drawing tests with amorphous carbon coated tools showed higher friction coefficients compared to lubricated tests without any coating and a high adhesive wear. A reduction of the contact ratio from 100% to 87.5% resulted in a decrease of the sliding friction value by 20%. Dry tribological ball-on-plate tests of different coatings against aluminum showed that a polished microcrystalline CVD diamond coating is most promising to enable dry aluminum forming with a long lifetime of the coated tool. By in situ silicon carbide sublimation in a diamond deposition process, a possibility has been demonstrated for atmospheric CVD processes to reduce the electrical resistance of CVD diamond layers without the use of toxic gases. The electrical resistance of the coating could be reduced with a silicon doping concentration in the order of 10^{20} cm^{-3} in range between 10^4 Ω and 10^6 Ω. Electrical discharge machining of CVD diamond coatings has been made possible by silicon doping, which means that the specific resistance has been reduced to below 100 Ω·cm.

Keywords: CVD diamond, friction, doping, ultrasonic vibration assisted milling, electrical discharge machining, microstructuring, sheet metal forming, dry metal forming, coefficient of friction

1 Background and motivation

The aim is to enable the dry forming of aluminum alloys during deep drawing by locally increasing the tool load capacity through the use of customized coatings. By local application and microstructuring of wear resistant carbon-based coatings on steel tools the dry deep drawing of aluminum sheets shall be made possible to the extent that the process limits are at the level of lubricant-based forming. In addition to coating, structuring in particular should improve the material flow and wear resistance of the used tools. In order to ensure scientific

*E-mail address of corresponding author: info-mbs@bias.de, Richard.boerner@mb.tu-chemnitz.de, peter.scholz@iwu.fraunhofer.de

comparability, commercially available amorphous carbon layers (a-C) should be considered to the same extent. Within the framework of the project, it has been proven that a pre-structuring of the substrate, the application of an appropriate coating and a microstructuring of the coated tools lead to a longer tool life, less material abrasion and an improvement of the component quality in terms of dimensional accuracy and structural fidelity.

A major challenge in the production of the forming tools is the coating of steel (X153CrMoV12-1, carbon content 1.53 wt%) with diamond. The deposition of diamond layers as well as the previous deposition of intermediate layers is to be carried out by a laser-based plasma chemical vapor deposition (LaPlas-CVD) process. There are many publications on the diamond coating of steel, which differ in the steel grade selected and the intermediate layer used. Fig. 1 summarizes the results of the different investigations. It should be noted that a steel grade with a carbon concentration higher than 1.27 wt% has never been coated and that the highest successful coating temperature was 920 °C.

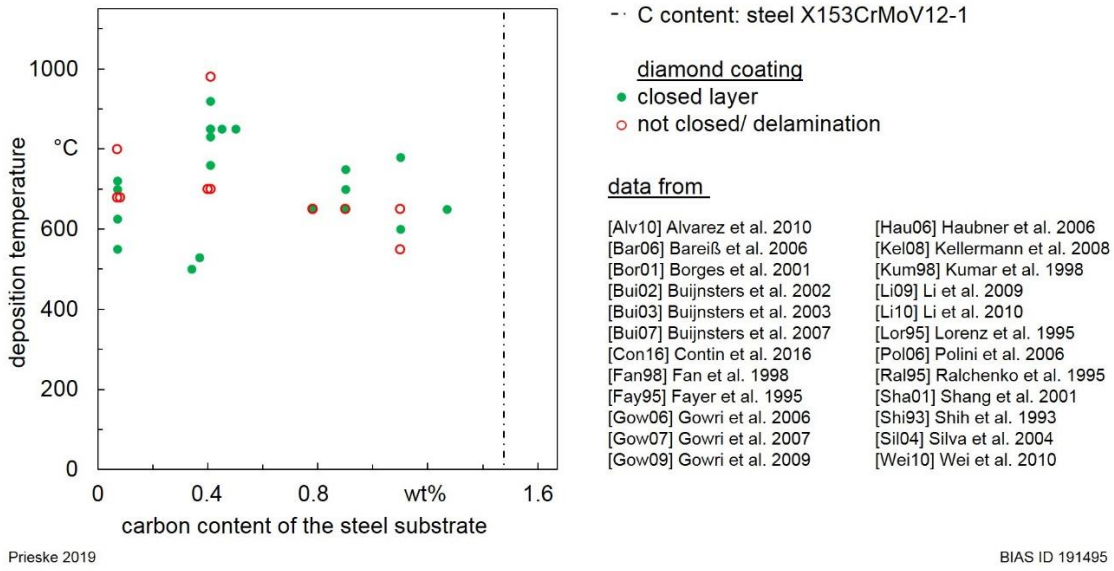

Fig. 1: Literature research on diamond coating of steel, wherein the coating temperature is plotted against the carbon content of the steel.

The LaPlas-CVD process enables the in-situ introduction of impurities. It is to be investigated whether the electrical resistance can be reduced by doping the diamond coatings in order to enable subsequent structuring and smoothing of the diamond coatings by means of electrical discharge machining.

The residual stresses within a deposited CVD diamond (CVDD) coating with a PVD diffusion barrier on steel, acts as a preload and can lead to spalling of the layer by applying an additional load during the forming process. The aim is to achieve a favorable residual stress condition in the substrate layer system and thus to ensure good adhesion even under loads typical for forming processes. The relationship in particular between the layer adhesion of CVDD and the substrate microstructure has already been investigated for numerous substrate materials. The effect of the substrate roughness on the CVDD coating of Si_3N_4 specimens was reported by Amaral et al. [1]. The combination of different pre-treatments and seeding processes led to the conclusion that surfaces roughened by plasma etching increase the layer adhesion of the CVDD coating due to "anchoring effects", whereby no closer information on the substrate roughness was given. Singh et al. observed that the generation of a three-dimensional (3D) thermally and compositionally graded interface between diamond and the substrate material leads to improved adhesion of the CVDD [2]. Under Wako et al. investigations were carried out regarding the layer adhesion of CVDD coating on differently pre-treated molybdenum specimens (99.9% Mo) [3]. The molybdenum substrates were pre-treated by polishing and grinding to achieve both different roughness combined with anisotropic and isotropic surface microstructures, respectively. The substrates with the higher surface roughness showed a better layer adhesion. In addition, it was concluded that anisotropic structures let a crack pass only in one direction, while isotropic structures tend to exhibit circular layer delamination in a stress test. Investigations on the influence of the surface roughness on the layer adhesion were also done under Xu et al [4]. In this case, CVDD coatings were deposited on cemented carbide substrates with smooth as well as blasted surfaces using a Cr-CrN interlayer system. While the diamond coating of the specimens without any interlayer system flaked off directly during cooling, adherent CVDD with a layer thickness of approx. 9 µm was deposited on both substrate microstructures with diffusion barriers. In a

Rockwell-C indentation test the diamond coating without surface pre-treatment showed significantly poorer attachment, which was shown through delamination at the interface to the interlayer. Thus, it could be concluded, that increased surface roughness values prior to CVDD coating enhances layer adhesion. Gomez et al. found in cutting experiments that a preferential direction of the substrate roughness, resulting from the delivery state or the finishing of the cemented carbide inserts, has a negative impact on the subsequent adhesion of the CVDD coating layer (> 20 µm) under mechanical stress [5]. By means of a more intensive mechanical interlocking and a mechanically graded transition from the substrate material into the CVDD coating, the compressive stresses in the transitional area can be significantly reduced compared to a smoother substrate surface. This was found by Lee et al. in their investigations in the CVDD coating of laser induced micro-rough surfaces on cemented carbide substrates [6]. Grögler et al. concluded generally in numerous research studies, that grit-blasting as well as grinding of substrate surfaces are favored methods for CVDD coating adhesion in case of deposition on titanium substrates [7, 8, 9, 10]. The roughness of the pre-treated surfaces was between 0.5 µm to 1 µm (ground) and 3 µm (grit-blasted). They attributed this primarily to the effects of mechanical interlocking as well as elastic deformation, which leads to a reduction of thermally induced residual stresses. Similar results in the CVDD coating of pure titanium were also be achieved by Lim et al. [11]. They concluded that a strong stress relaxation within the applied diamond layer could be affected by corundum blasting and etching roughened substrate surfaces. This may be due to the fact that layer thickness and substrate roughness are of the same order of magnitude about 3 µm to 5 µm. Here, the diamond layer is strong enough to prevent the contraction of the roughness peaks during cooling after the deposition process. As a result, only weak thermal compressive stresses arise within the layer.

The generation of a defined fine microstructure on the substrate surface should contribute to layer adhesion and residual stress compensation. Furthermore, the relationships between the characteristics of microstructuring (e.g. contact ratio) on forming tools and the material flow of the workpiece are to be determined and understood.

2 Methods and materials

A CO_2 laser-based plasma CVD process, shown in Fig. 2 was used at atmospheric pressure without a vacuum chamber for the deposition of polycrystalline CVD-diamond coatings. A 6 kW high-power CO_2 laser with a wavelength of 10.6 µm was used for energy supply of the plasma jet. The ignition chamber was flooded by argon gas through a gas nozzle. The ignition of the plasma flame was achieved by thermionic emission through inserting a tungsten lanthanum ignition rod into the laser focus. This generates an optical breakdown. After the ignition of the argon plasma flame, the process gases (0.02 standard litres per minute (slm) methane and 1.98 slm hydrogen), which are required for CVD synthesis of polycrystalline diamond, are supplied.

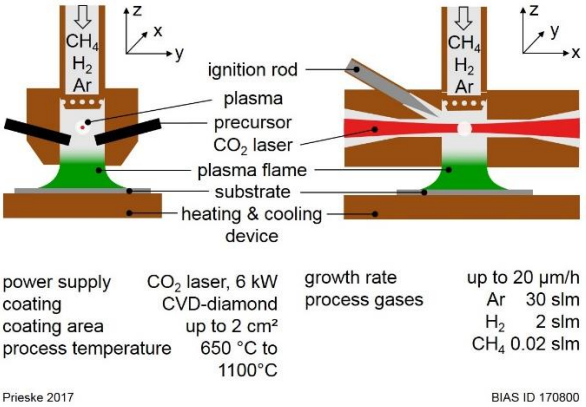

Fig. 2: Schematic layout of the laser induced plasma CVD process at atmospheric pressure.

To ensure a constant deposition temperature over the whole deposition time, a feedback control was implemented, which regulates the laser power according to the measured substrate temperature of the IMPAC pyrometer IGAR 12-LO. Detailed information of the implementation of the feedback control are published in [12]. For temperature monitoring, three pyrometers were used, IMPAC pyrometer IGAR 12-LO, IP 140 and IGA 10. To determine the emission coefficient for each pyrometer for different substrates, the substrate was heated up to 800 °C by a ceramic hot plate and the surface temperature was measured by a thermocouple. The emission coefficients were set accordingly so that each of them measures the same temperature as measured by the thermocouples.

As substrates for the different investigations molybdenum sheets with a purity of 99.97% and a thickness of 1 mm, K10 tungsten carbide plates with a Cobalt content of 6% and a thickness of 3 mm and steel of material number X153CrMoV12-1 with a thickness of 3 mm are used. The tungsten carbide substrates where etched by Murakami reagent ($K_3Fe(CN)_6$: KOH : H_2O = 1:1:10) for 30 min and subsequently with Caro's reagent (3 mL 96 wt % H_2SO_4, 88 mL 40% w/v H_2O_2) for one minute [13]. Diamond nucleation was carried out with a dispersion consisting of 200 ml of isopropanol and 210 mg of diamond powder with an average crystal size of 0.25 µm to 0.50 µm from the company Microdiamant AG. The substrates were put into the dispersion for ten minutes in an ultrasonic bath and subsequently into isopropanol for three minutes. To characterize the process window for the deposition of CVD diamond coatings with the LaPlas CVD process, 72 different deposition parameter sets were applied for process temperatures from 650 °C to 1100 °C and methane concentrations from 0.15% to 5.0%. The temperature was increased in 50 K steps.

As precursors for the in-situ evaporation two different types of rods are used. Solid silicon carbide (SiC) bars (high-tech ceram®-SSiC) with a squared cross-section, a side length of 2.1 mm and purity higher than 99%. Furthermore, aluminum oxide (Al_2O_3) rods (CC ceramic components e.K.) with a diameter of 3 mm and a purity of 99.7% are used as precursors. The precursors are inserted by feed units using DC-servomotors with a positional accuracy of 0.1 mm. The amount of sublimated material was kept constant during CVD diamond deposition by keeping the intensity of the corresponding peaks in the measured emission spectra constant through feeding the precursor into the plasma flame. To examine the influence of different surface microstructures the structured steel specimens are coated by the company Oerlikon Balzers with a 2.4 µm thick chromium nitride (BALIQ® CRONOS) layer by high-power impulse magnetron sputtering (HIPIMS) in one batch. The thickness and the type of coating were chosen regarding to the publication of Buijnsters et al. [14]. A high CrN interlayer thickness of 20 µm as used by Glotzman et al. [15] was avoided to be able to evaluate the impact of the microstructure on the adhesion of the diamond coating.

Scanning electron microscopy (SEM) (Carl Zeiss Microscopy EVO MA-10) and 3D laser microscopy (Keyence VK-9710 and Keyence VK-9700) were used to take images of the surface and to determine the roughness parameters according to ISO 25178 part 2 and 3 on a measuring area of 0.5 mm × 0.5 mm. This ensures that a minimum of five form elements in both the X-direction and the Y-direction are included in the calculation of the surface parameters. For the roughness analysis an S-Filter of 2 µm and an L-Filter of 0.5 mm was used. Element analysis was done by an energy-dispersive X-ray spectroscope (EDX) (Bruker Nano GmbH XFlash Detector 610M). Micro Raman spectroscopy (Renishaw system 1000) was employed to evaluate the existence of diamond films and amorphous carbon coatings using an excitation wavelength of 514 nm. The spot size of the laser beam was 10 µm in diameter and the spectrometer has a spacial resolution of 1.6 cm^{-1}. The existence of diamond was evidenced by the measurement of the first order Raman line of diamond at 1332 cm^{-1} [16]. To study the micro- and nano-topography within the wear tracks after tribometer tests atomic force microscopy (AFM) was carried out. The used AFM device Nanoscope III of the company Digital Instruments works in tactile mode and has a resolution of 1 nm in vertical and 10 nm in lateral direction. Cryofractures were produced by eroding a predetermined breaking point into the substrate up to 0.5 mm underneath the coating area. Afterwards the specimen was cooled down by liquid nitrogen and broken into two parts. Dilatometer measurements at steel specimen were performed with a quenching dilatometer DIL 805A according to ASTM A1033-10. The steel specimens for the dilatometer tests were used in form of pipes and had a length of 10 mm, an outer diameter of 4 mm and an inner diameter of 3 mm.

To determine the influence of an in situ impurity introduction in diamond on the electrical resistivity, 2-point resistance measurements were executed using a Fluke 117 multimeter with a measuring tip distance of 2 mm. At the Fraunhofer ISC in Würzburg (Germany) four-point probe van der Pauw resistivity measurements have been executed. Four contacts have been arranged on a single diamond crystal. A power I has been applied at two neighboring contacts and the voltage was measured at the other two contacts. The contacts have been cyclically exchanged. The sheet resistance ρ was then calculated using the van der Pauw method [17].

To determine the coefficient of friction and wear, different carbon-based layers were investigated in the oscillating ball on plate tribometer test without the use of lubricants. For the investigations the CETR Universal Tribometer UMT3 with a surrounding climate chamber, which kept the environmental conditions constant at a temperature of 24°C ± 1°C and 40% ± 1% relative humidity, was used. The tests were carried out according to DIN EN 1071-12 [18]. Aluminum balls of the alloy AlMg4.5Mn0.7 (EN AW-5083) with a diameter of 10 mm were used as counter bodies. To examine the long-term behaviour of different carbon coatings and surface conditions, a total sliding distance of 1 km was chosen, corresponding to 99,900 cycles along a linear

sliding length of 10 mm. The velocity was set to 50 mm/s and the contact force was set to 10 N ± 0.2 N leading to Hertzian contact pressures around 700 MPa, which are typical sheet metal forming conditions [19]. Fig. 3 shows the different surfaces tested in the oscillating ball on plate test. In order to identify mirror-smooth surfaces, the BIAS logo mirror image was printed on paper and positioned behind the sample. The following layers were tested: polycrystalline CVDD layers, mechanically polished CVD diamond layers (pCVDD), polished steel substrates of material number X153CrMoV12-1 and a-C:H:W /a-C:H (a-C:H) coating system with a thickness of 2.2 µm on polished steel (in cooperation with the SPP 1676 project TRUK - Potentials of dry swaging). The steel substrates were austenitized at 1080 °C for about one hour, quenched in oil and then tempered three times at 500 °C for about 30 minutes at each tempering step. This heat treatment results in a required overall tool hardness of about 60 ± 2 HRC determined by Rockwell indentations corresponding to a micro-hardness of about 900 HV1.

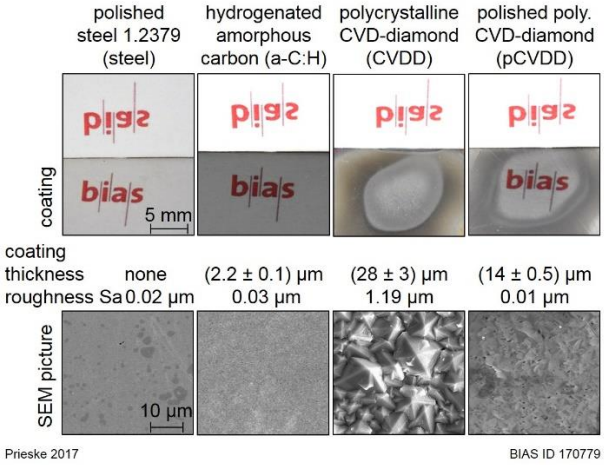

Fig. 3: Photo (top) and scanning electron image (bottom) of the surfaces examined in the ball on plate test.

The Vickers hardness of the used materials was determined by a Fischerscope H100C universal micro-hardness device of the company Helmut Fischer GmbH according to DIN EN ISO 14577-1 [20]. The set normal load of 10 mN respectively 1 N is depending on the surface roughness and coating thickness. The hardness of the CVDD sample could not be measured due to the high roughness of the surface and low indentation depth. Due to the same plasma CVD process parameters for the deposition of the diamond coatings it is assumed that the hardness results are the same as for the pCVDD and the CVDD coating. The results of the hardness measurements are shown in Tab. 1.

Tab. 1: The Vickers hardness HV of the surface of the different samples as well as the aluminum counter material.

	steel	a-C:H	CVDD and pCVDD	EN AW-5083
hardness	903 HV0.01	1894 HV0.01	11525 HV1	151 HV1
standard deviation	46 HV0.01	124 HV0.01	225 HV1	10 HV1

The Hertzian pressure for the different plates against the aluminium alloy ranges from 623 MPa for a-C:H coating to 759 MPa for the diamond coating.

The test tools shown in Fig. 4 were used for the comparative tribological investigations (strip drawing tests) and forming tests (cupping tests). Within the priority program it was specified that active parts have to be manufactured from the cold work steel X155CrMoV12, hardened to (58 + 2) HRC commonly used in sheet metal forming. With regard to the coating to be applied on the active part surfaces, a surface roughness of Ra = 0.02 µm was defined. At the beginning, tribological investigations were carried out with samples of the aluminum alloy EN AW-5182-H111 in 1.0 mm sheet thickness. The microstructuring of the tool surface to influence the contact area and thus the variation of the effective surface pressure was realized at the Professorship Micromanufacturing Technology by milling. Subsequently, the DLC coating (amorphous carbon layer) of the correspondingly processed tool parts was carried out externally by a contract coater.In addition to the commercially available DLC layer, a multi-layer system developed in the project "Potentials of Dry Rotary Swaging" by IWT Bremen was randomly examined as part of a cross-project collaboration. Due to shortcomings in the coating process, the local coating of the tools with CVD diamond could not be realized within the project.

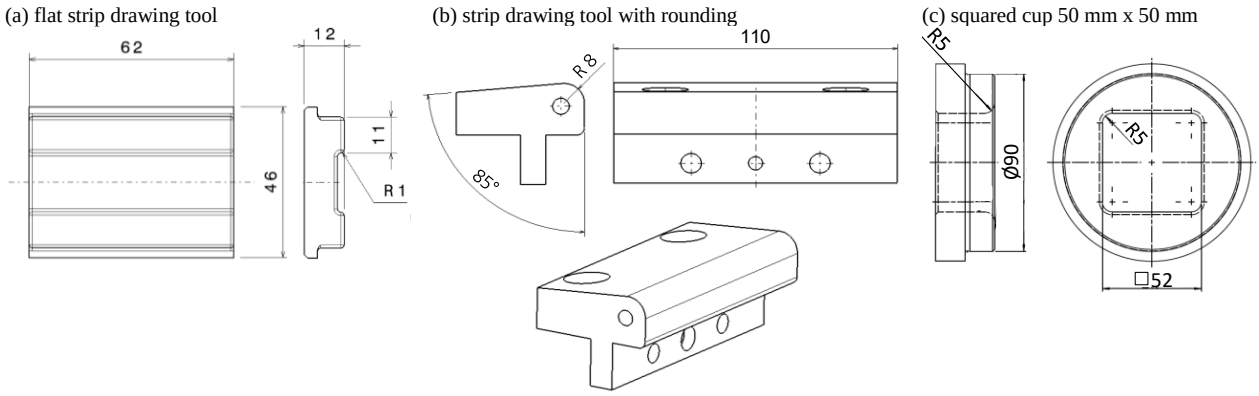

Fig. 4: Overview of the test tools – strip drawing test (a, b) and deep drawing test (c)

Using the strip drawing test with flat drawing tools enables simulating the tribological system between blank holder and sheet metal. The sheet metal, fixed on a sliding device, was pulled under the drawing tool loaded with a normal force F_N (Fig. 5). No tangential force application was used. The friction force F_R was determined by a measurement device. Assuming COULOMB friction, the coefficient of sliding friction µ was calculated. The applied velocity (v_{str} = 50 mm/s) is in typical ranges of common deep drawing processes. The coefficients of friction µ were determined for seven different normal pressures from 1 MPa to 17 MPa. The test conditions and the test matrix are shown in Tab. 2 and Tab. 3. The reference tests were made using lubrication.

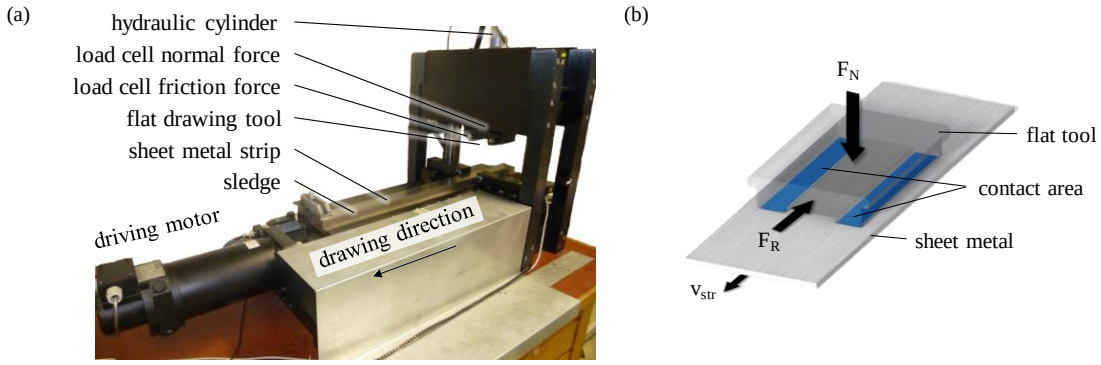

Fig. 5: Experimental set up (a) and principle (b) of the strip drawing test with flat tools

Tab. 2: Experimental matrix strip drawing test (flat tool)

tool coating	uncoated	coated			
tool structuring	without	without		structure with 75 % contact area	structure with 87.5 % contact area
lubrication condition	lubricated	dry	lubricated	dry	dry

Tab. 3: Experimental conditions strip drawing test (flat tool)

strip	EN AW-5182-H111, electro discharge textured (EDT) surface, drawing direction was parallel to the rolling direction, delivery condition dry and clean; t = 1.0 mm, width 50 mm, length 1000 mm
tool	1.2379, completely hardened (58 + 2) HRC, ground and polished, functional surfaces: Ra < 0.02 µm
drawing additives	Lubrication applied using a roller, ca. 2 g/m² WISURA ZO 3368
reference coating	a-C:H:Si; thickness of coating: 2 µm ± 0.5 µm
IWT-coating	a-C:H/a-C:H:W multilayer system; thickness of coating ca. 2.2 µm

By using the deflected strip drawing test with round tools (Fig. 6), the friction conditions at a simply curved drawing edge can be simulated during deep drawing. The test matrix and the test boundary conditions correspond to those of the flat strip drawing test (see Tab. 2 and Tab. 3). However, the drawing path in the strip drawing test with deflection is only approx. 300 mm. Three load horizons were investigated to determine the influence of the surface pressure on the wear behavior. In contrast to the flat strip drawing tests, the rectangular pattern was rotated at an angle of 45° to the drawing direction. Spot tests with the IWT coating were not carried out.

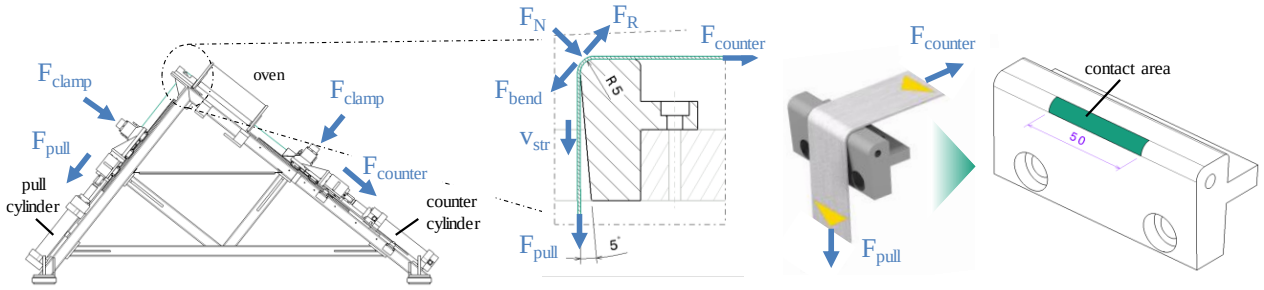

Fig. 6: Experimental set up and principle of the deflected strip drawing test with round tools

For the transfer of the findings from strip drawing tests, a modular forming tool for the production of squared cups was used (Fig. 7). The tool is designed in such a way that the active parts made of X155CrMoV12, hardened to (58 + 2) HRC can be easily exchanged according to the above-mentioned tests. With the help of this test on a laboratory scale, the load-dependent behavior of the CVD diamond layer during the deep drawing process under dry conditions was to be investigated. Since BIAS could not provide any CVD diamond coated active parts, only spot tests with coated (a-C:H:Si) and uncoated tools were carried out under lubricated and dry conditions. Due to the results of the basic strip drawing tests, the active parts were not structured.

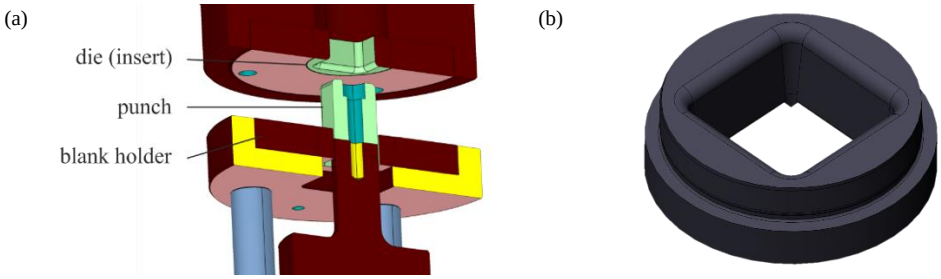

Fig. 7: (a) CAD-model of the cupping test tool and (b) exchangeable insert of the drawing die

Both the structuring for the tribological functional surfaces of the tools for strip drawing tests as well as the microstructuring of the steel specimen for a subsequent CVDD coating were done in the high precision machining center KERN Pyramid Nano. In order use the ultrasonic vibration assistance experimentally, the implementation of a corresponding device became necessary. The vibration excitation was carried out on the workpiece side due to the available system technology. A generator type UIP2000hdT with the associated transducer equipment from Hielscher was implemented on the machine table. Via a connecting element it was coupled with a cross converter, which on the one hand deflects the direction of the vibration by 90° and on the other hand takes up the workpiece by a screw connection (fine thread: M14 x 1). The test specimens made of X135CrMoV12-1 were examined both in the soft annealed condition (255 HB) and hardened (60 HRC). Their geometric design was made for resonant vibration, which meant that they were only allowed to have a comparatively low weight and height. A hexagonal profile with a width across flat (WAF) of 32 mm enables a tightening torque of 150 N m (for the soft annealed condition) and 50 N m (for the hardened condition). These torques were applied for the investigations, to secure a sufficient coupling. For the measurement of the amplitudes, a single-point laser-vibrometer (Polytec OFV-505) was used, while the incoming signal was analyzed by an oscillator with the associated software (PicoScope® 2000 Series). In ultrasonic vibration assisted face milling the relative motion of the tool and the workpiece is a combination of the tool feed motion, the tool rotation and the ultrasonic vibration. In the experimental setup the direction of the ultrasonic vibration coincides with the rotational axis of the tool and it is perpendicular to the workpiece surface and the feed direction, respectively (Fig. 8). The wavelength λ indicates the structural distance on the path of the tool circumference and is calculated from the ratio of the ultrasonic frequency f_{US} and the cutting speed v_c.

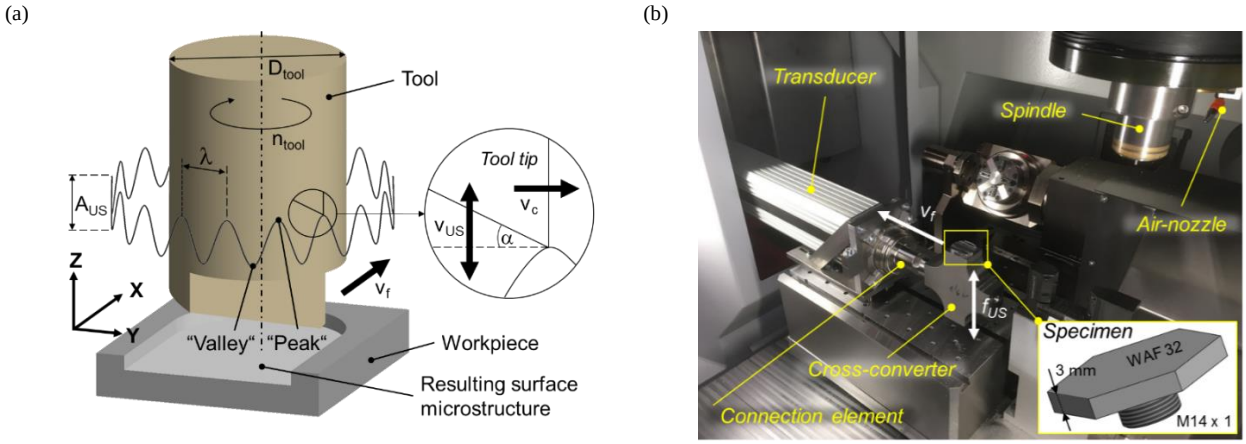

Fig. 8: Kinematics of ultrasonic vibration assisted face milling (a) and experimental set-up for UVAM (b)

The amplitude of the relative motion between the tool and the specimen had to be determined for the generation of the surfaces with a predefined microstructure. Therefore, the relation between generator output power and the amplitude A_P, which is half of A_{US} (peak-peak) achieved at the specimen surface was examined before the experiments. The set point value for the amplitude at the generator was increased in increments of 10 % and the amplitudes were determined on the specimen surface by a measurement with a laser vibrometer in order to check the performance of the system in an idle state, Tab. 4. Slight deviations of the measured values are attributed to the transmission characteristics of the oscillation system. The vibration amplitude was transformed in the direction perpendicular to the tool axis (f_{US}, Fig. 8). During the process, an additional piezoelectric disc is used as a sensor element. The measured signal is processed within the control circuit to ensure operation in resonance mode. The resonant frequency f_{US} was about 19.2 kHz.

Tab. 4: Measurement of the amplitudes of the oscillation system using a laser vibrometer (maximum set point value ≙ 10 µm at 100 %)

Set point value	Amplitude A_P
20 %	1.8 µm
30 %	3.3 µm
40 %	4.5 µm
50 %	5.7 µm
60 %	6.6 µm

For the electrical discharge machining (EDM) experiments, the 3-axes micro EDM machine SX100 HPM of the Swiss manufacturer Sarix was used, Fig. 9 (a). The system provides a relaxation generator, which enables pulse discharge periods in a range of 70 ns to 1000 ns. The properties of the electric discharge pulses were controlled by the parameters open-circuit voltage U0, the discharge power level CF, pulse frequency FR and pulse width WH. The Fig. 9 (b) provides a detailed view of the working area and the basic setup used for all experiments. As tool electrode WC-Co rods with a diameter of 90 µm and a rotation speed of 600 rpm were used. The coated diamond workpiece was clamped and electrically contacted with an appropriate dimensioned bench vise. A lateral flushing of oil HEDMA111 from Oelheld was used as dielectric fluid. Fig. 9 shows the used micro electrical discharge machine as well as a detailed view of the working area.

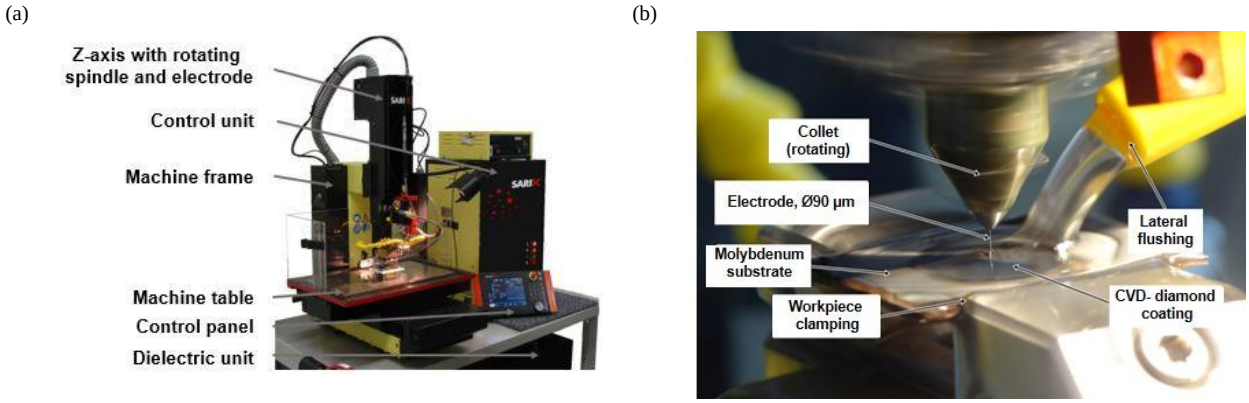

Fig. 9: Micro EDM machine Sarix SX100 HPM (a) and detail view on the working area for EDM of CVDD layers (b)

For the machining of micro-bores with a target depth of 50 µm, the open-circuit voltage was varied from 90 V to 150 V. Discharge power levels from CF100 to CF105 (equivalent to 5.9 µJ to 38.5 µJ at 150 V) were applied and tool polarity was varied too. The reproducibility was analyzed by each five experiment repetitions.

Boron doped diamond material samples were investigated for electrical discharge machinability. For this purpose, a massive boron doped diamond material CVDITE CDE from ElementSix and an electrode coated with a 12 µm thick boron doped diamond layer from the company DiaCCon were experimentally analyzed. The experiments were conducted by varying open circuit voltage, discharge energy level and tool polarity in analogy to the silicon doped CVD diamond experiments.

In order to analyze the effect of the surface microstructure on material flow during forming process, the micro EDM process has to be designed to allow for smoothening of the CVD diamond layer by generating defined and reproducible surface roughness. Arrays were machined into doped diamond layers by path erosion. For this purpose, the setup known from Fig. 9 was used and adjoined paths with a lateral distance of 50 µm (correlating to 45% of path coverage) and a target depth of 8 µm were machined in both, silicon and boron doped CVD diamond layers. An open-circuit voltage of 130 V and a negative tool polarity was applied, and the discharge energy was varied in a range of 2.6 µJ to 13.7 µJ for silicon doped CVD diamond layers and up to 18.1 µJ for boron doped CVD diamond layers.

3 Results

Stress analysis in deep drawing

To analyze the stresses acting on the tool surface during deep drawing, FE simulations of the squared cup were carried out at Fraunhofer IWU (Fig. 10a). Due to the symmetry of the geometry only ¼ of the component was simulated (Fig. 10b). The simulation in the worst-case scenario (coefficient of sliding friction $\mu = 0.3$, blankholder force $F_{bh} = 15$ kN) showed that the greatest stresses on the die surface occur in the area of the radius and in the corners (10b). Locally, absolute values of the surface pressures of up to 150 MPa (Fig. 10c) were effective in these areas. The coating system must be able to withstand this stress perpendicular to the tool surface in order to reduce potential wear.

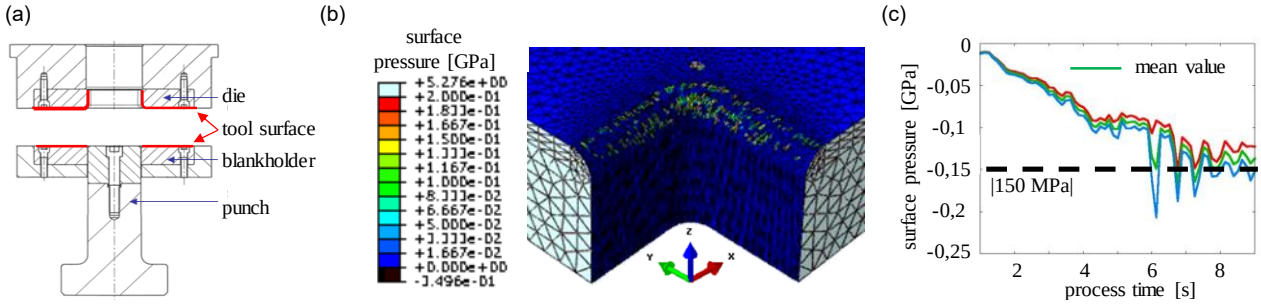

Fig. 10: Stress analysis deep-drawing (a) drawing of the cupping test tool; (b) FE model of the die, (c) surface pressure on the surface of the die over time

FE simulation with locally variable coefficients of friction

Within the scope of the project, microstructuring of the tool surfaces is primarily intended for setting tribological effects. The possibility to adjust the coefficient of friction locally by microstructuring the surface of the forming tools allows the targeted control of the material flow, which is of particular interest for deep drawing of complex geometries. As the stress analysis in Fig. 10b has shown, the greatest stresses occur in the area of the drawing edge. For this reason, it is important to keep the friction as low as possible there.

To estimate the influence of locally different coefficients of friction on the drawing result, a corresponding FE model with five different variants was simulated (Fig. 11). In each variant the distribution of the coefficient of friction is shown for the die side. The coefficients of friction of the blankholder are distributed mirror-inverted to the die. Variant 1 is used as a benchmark. In this variant, the coefficient of friction is assumed to be constant over the entire blankholder and die surface and only varies globally (μ = 0.05; 0.1; 0.3). In contrast, in variants 2 and 3, the flange area and the die radius are segmented and provided with different coefficients of friction. In variant 4 the die radius has a lower coefficient of friction than the flange area. Whereas in variant 5 only the corner areas of the die radius are provided with a reduced coefficients of friction.

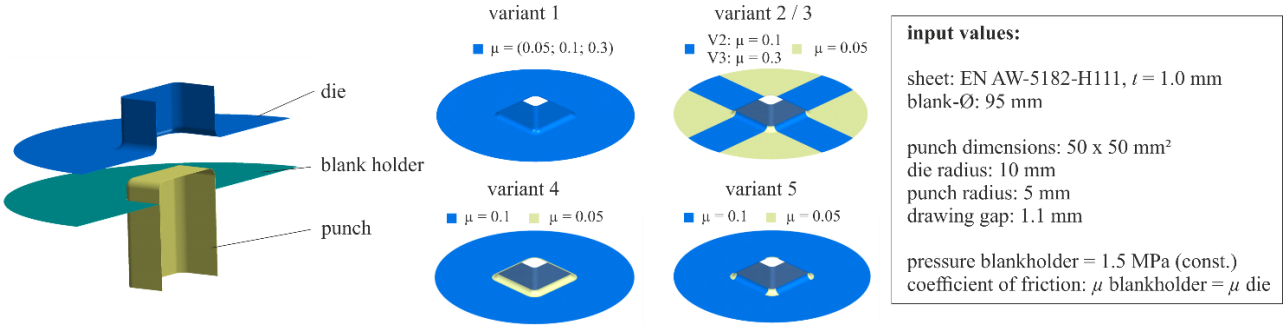

Fig. 11: FE model for the cupping test with locally variable coefficients of friction (variants 1 to 5)

The maximum drawing depth, the drawing force or forming energy and the sheet thickness distribution were used for evaluation and comparison. The drawing process was always performed until the sheet material failed. The mechanical properties of the sheet material were determined experimentally by tensile tests and Nakajima tests.

The results using variant 1 as an example show that, as expected, the drawing depth decreases as the coefficient of friction increases (Fig. 12a). As a result of the increased frictional forces, there is an analogous increase in the drawing force. The highest drawing depth was achieved with variant 3. The local increase in the coefficient of friction in the straight sides of the drawn part leads to an increase in the drawing force and thus to a slowing down of the material flow. In combination with reduced coefficients of friction in the corner areas, this results in a more favorable stress distribution in the workpiece. Consequently, the more homogeneous stress distribution enables larger drawing depths than with variant 1 (μ = 0.05). A similar effect is achieved when using draw beads to control the running-in behavior of the sheet material.

This effect also applies to variant 5 in a mitigated form. Due to the reduced coefficient of friction in the corner areas of the die radius, the drawing depth can be slightly increased compared to variant 1 (μ = 0.1). This effect can also be observed with variant 4, in which the die radius is provided with a reduced coefficient of friction all around. If the forming energy is normalized to the drawing path (Fig. 12b), the example of variant 3 shows that the local increase of the coefficient of friction for the same drawing path also leads to an increase of the necessary forming energy compared to variant 1 (μ = 0.05). The reduction of the necessary forming energy due to a reduction of the coefficient of friction in the area of the die radius is negligible.

The evaluation of the sheet thickness distribution at maximum drawing depth in Fig. 13 shows no significant differences between the individual variants.

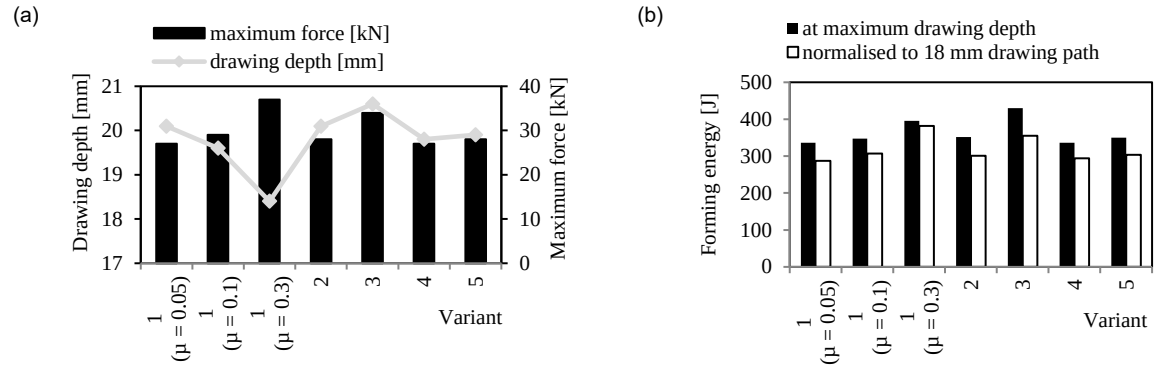

Fig. 12: FE simulation cupping test (a) comparison drawing depth and drawing force, (b) forming energy

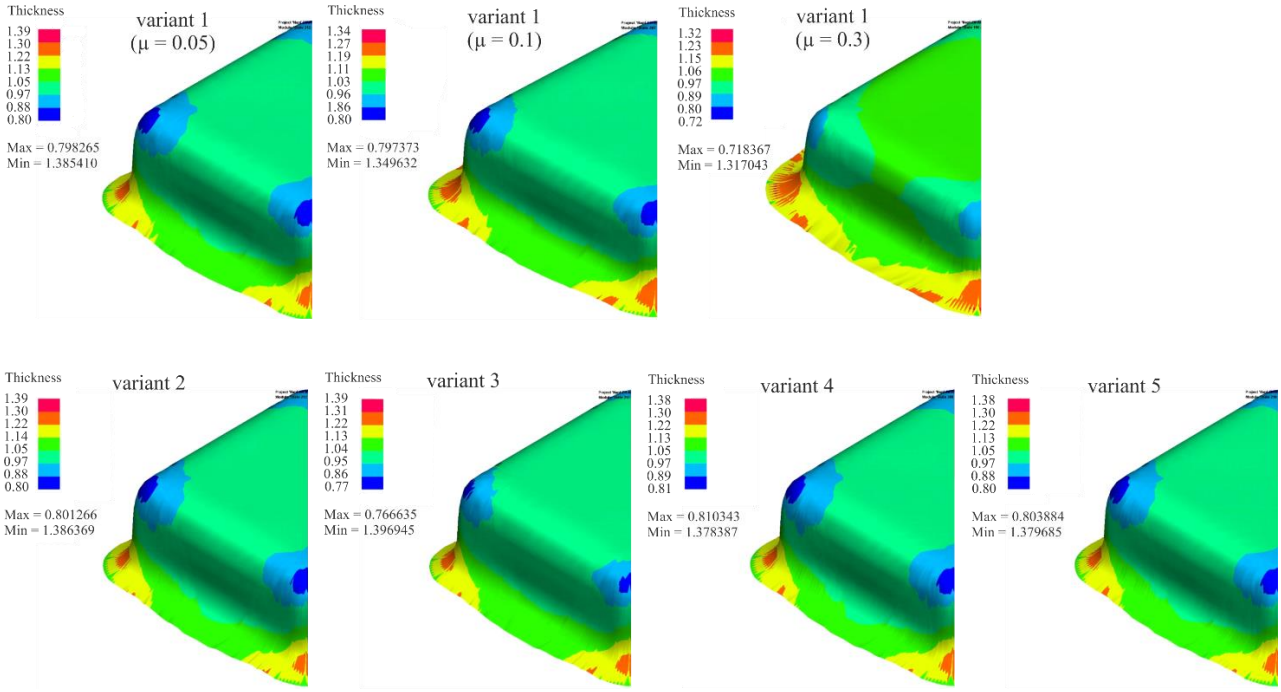

Fig. 13: Sheet thickness distribution from FE simulation at maximum drawing depth

Flat strip drawing tests

The diagram in Fig. 14a shows the coefficient of friction over the normal pressure for the reference strip drawing tests with uncoated, a-C:H:Si-coated (reference) and a-C:H/a-C:H:W-coated (IWT), unstructured drawing tools against EN AW-5182-H111 under the use of lubrication (2 g/m²). With both drawing tools 35 strips were drawn in each case (five strips per normal pressure). In comparison to the uncoated drawing tool the coefficient of friction for using the coated drawing tool decreases significantly less with increasing normal pressure. This can be explained by the fact that the surface structure of the drawing tool was preserved by the hard a-C:H:Si coating and thus no distinct smoothing during the drawing process could take place. With the IWT coating, aluminum adhesion occurred towards the end of the test series. These explain the increase in the coefficient of friction with increasing surface pressure.

On the functional surfaces of all drawing tools abrasive traces of wear could be detected after the experiments. The wear pattern was distributed homogeneously over the complete width of the functional surface of the uncoated drawing tool. In contrast, only a few scratches were visible on the drawing tool with the reference coating due to the higher hardness and strong wear resistance of the amorphous carbon layer (Fig. 14b). However, the occasional scoring indicates a locally limited premature failure of the coating. It can be assumed that in these regions hard abrasive particles from the aluminum oxide layer of the metal strip led to a local overloading of the layer. On the IWT coating strong adhesion signs on one edge of the functional surface were visible at the end of the tests.

The sheet metal surfaces that were exposed to the functional surfaces of the drawing tools show a uniform smoothing, which is visible through the changes in the degree of gloss (oblique illumination). A difference

between the sheet surfaces which were mechanically stressed with the coated and uncoated drawing tools cannot be seen. Abrasive or adhesive wear marks are not present on both strips. During the tests with the IWT coating, slight abrasive traces of wear were visible on the metal strips, which were subjected to a high surface pressure.

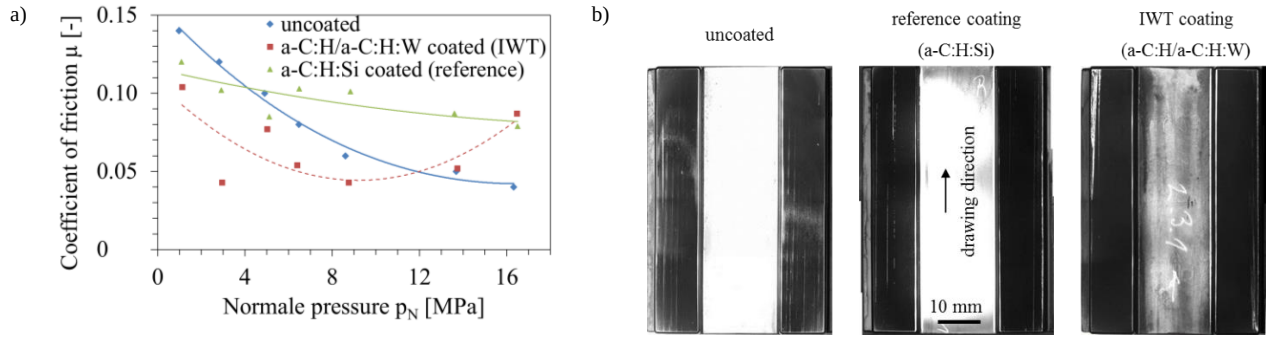

Fig. 14: a) Coefficient of friction over the normal pressure for the reference strip drawing tests with lubrication b) Overall view of the functional surfaces after testing.

The diagram in Fig. 15 shows the coefficient of friction (in average over the stroke) for the strip drawing tests under 1 MPa normal pressure with blank and coated drawing tools unstructured and microstructured (resulting in a reduction of the nominal contact area to 75% and 87.5% respectively) at dry and lubricated conditions. Without lubrication already after the first test at the lowest normal pressure (1 MPa), strong aluminum adhesion to the functional surfaces of the drawing tools occurred after a few millimeters of stroke for all variants (Fig. 16). As a result of the adhesive wear, there was a significant increase in the coefficient of friction compared with the lubricated tests. The analysis of the coefficients of friction showed that the unstructured coated drawing tools led to the largest coefficient of friction at dry conditions. The coefficient of friction for the coated drawing tools are unexpectedly even above the level of the uncoated ones. One reason could be the slower smoothing mechanism of the functional surfaces compared to uncoated active parts. The drawing tools microstructured with calottes showed a decreased coefficient of friction of approximately 22% for the reference coating and 8% for the IWT-coating. Due to the small differences in the coefficients of friction, it was not possible to clearly assign the influence of the contact area on the sliding friction coefficient.

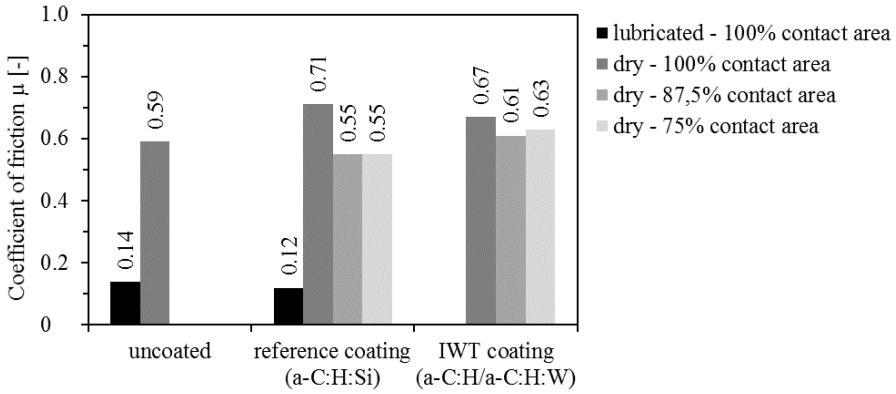

Fig. 15: Coefficient of friction at 1 MPa normal pressure – blank and coated steel unstructured and structured with 75% and 87.5% contact area at dry and lubricated conditions

The strongly increased coefficient of friction, in comparison to the experiments with lubrication, can be referred to the aluminum deposits on the drawing tools. As the drawing distance increases, the sheared aluminum accumulates from calotte to calotte (Fig. 16b), resulting in greatly increased sliding friction values. In some areas the calottes were overlaid with parts of the aluminum strips, so that the microstructures in these regions had no effect. The visual inspection of the sheet surface by light microscopy carried out after the strip drawing tests shows a clear scoring structure in the drawing direction. For applications with high quality requirements, such topographical changes of the sheet surface are not permitted.

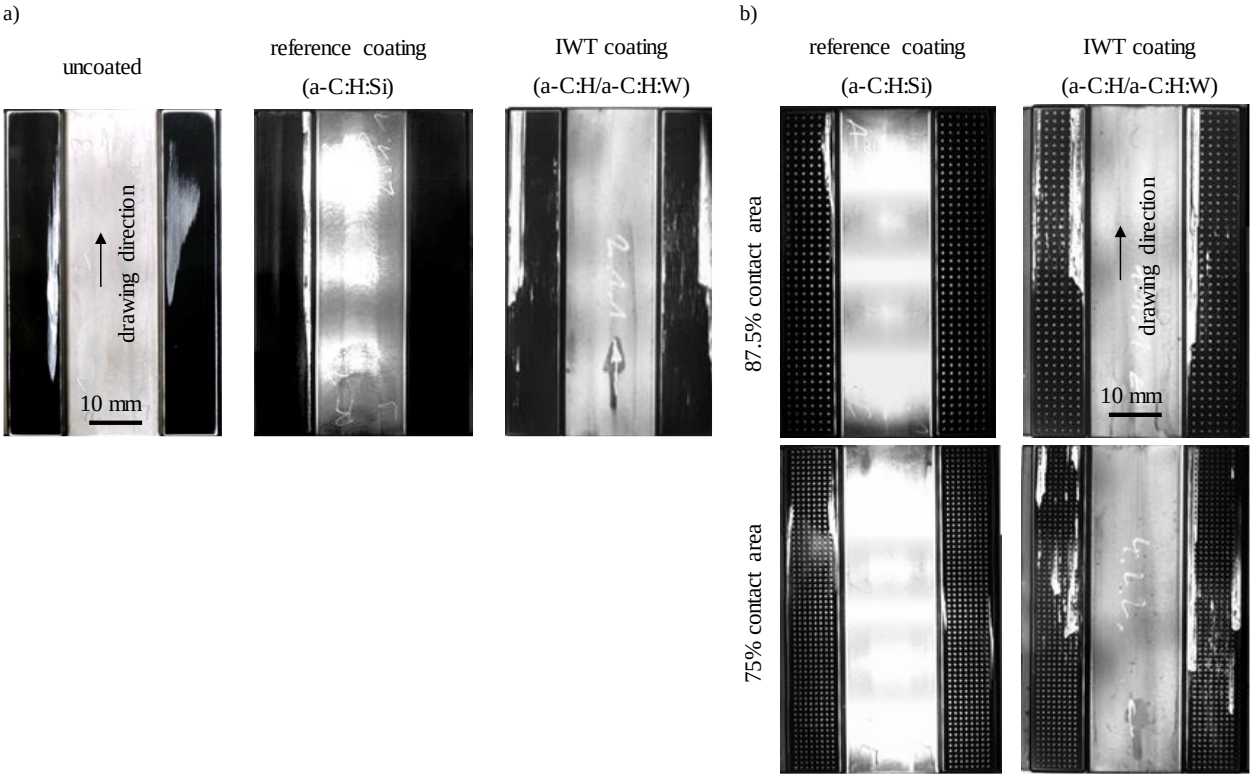

Fig. 16: Overall view of the functional surfaces after testing under dry conditions: a) unstructured functional surface b) structured functional surface.

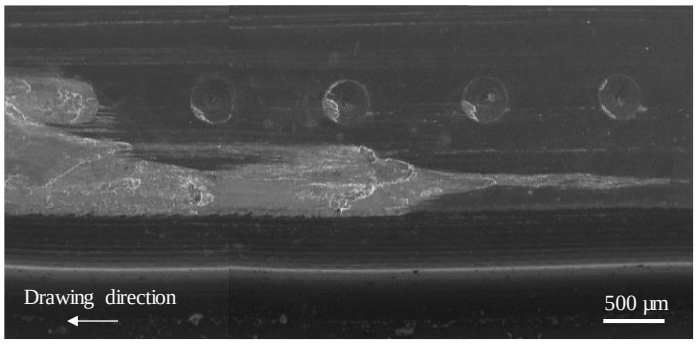

Fig. 17: Detail view of accumulated aluminum adhesions

Strip drawing tests with deflection

The subsequent strip drawing tests with 90° deflection confirmed the results from the flat strip drawing tests. In contrast to the flat strip drawing test, this test simulates the friction conditions at a single curved drawing edge during deep drawing.

The analysis of the coefficients of friction in Fig. 18 shows that the lowest coefficient of friction values were achieved under lubricated conditions, regardless of whether a coating is used or not. This is also reflected in the assessment of the functional surfaces (Fig. 19). In the tests with lubricant, slight aluminum adhesions are only visible in the edge areas. Without lubricant, large-area aluminum adhesions lead to a sharp increase in the coefficient of friction or to tearing of the sheet metal strip due to the friction forces acting, but at a lower level than in the flat strip drawing tests. In analogy to the flat strip drawing tests, the sliding friction coefficient could be reduced by approx. 20% at a surface pressure of approx. 10 MPa (Fig. 18a) by microstructuring (87.5% contact area), with an increasing tendency at an increase of the surface pressure (Fig. 18b and c). Contrary to expectations, however, the reduction of the contact ratio to 75% did not lead to a further reduction in the coefficient of friction. In conjunction with the results from the flat strip drawing tests, it can be assumed that an excessive reduction of the contact ratio has a friction-increasing effect.

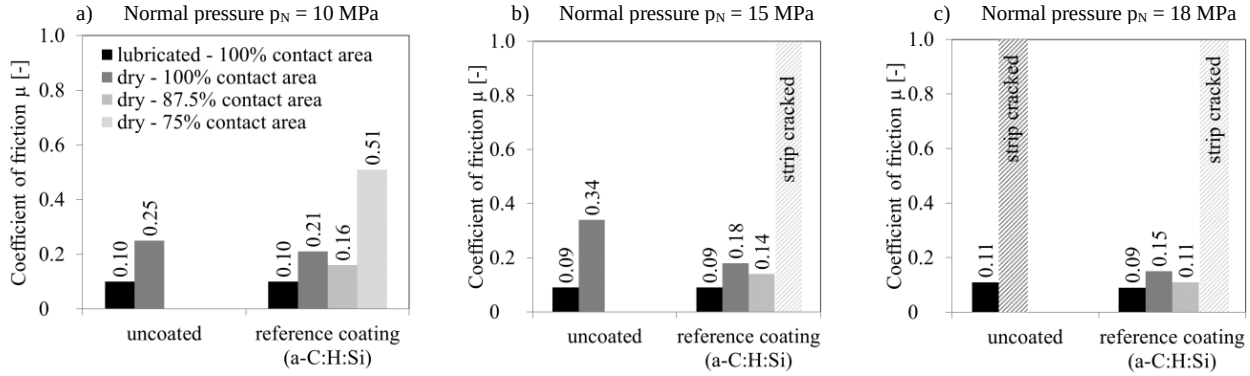

Fig. 18: Summary results of deflected strip drawing test, dry vs. lubricated at different normal pressures p_N

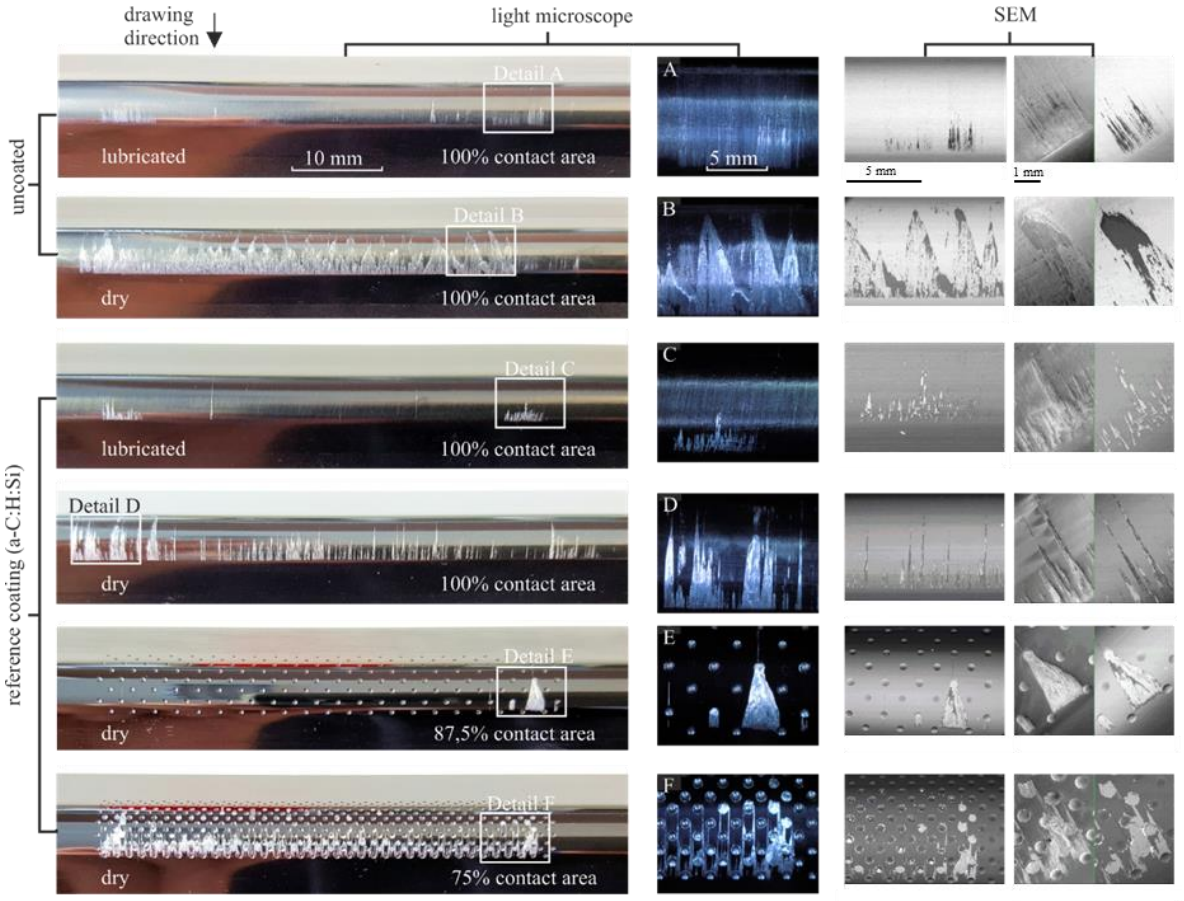

Fig. 19: Functional surfaces of the drawing tool after testing

In summary, it can be concluded that the coefficient of sliding friction can be reduced during dry forming by microstructuring and coating the drawing tool. However, the level of the sliding friction coefficients determined is clearly too high compared to lubricated forming due to strong adhesion of the aluminum alloy [21].

Cupping tests

The initial aim of this investigation was to transfer the tribological findings from the strip drawing tests to the construction small deep drawing tools. With the help of this laboratory-scale test, the load-dependent behavior of the CVD diamond layer during the deep drawing process under dry conditions was to be investigated. Since CVD diamond coated active parts could not be produced within the runtime of the project, only brief trials with DLC coated and uncoated tools were carried out dry and with lubrication. Due to the results of the basic strip drawing tests, the active parts were not microstructured.

For the test run, a forming tool for the production of rectangular cups was used, which is available at Fraunhofer IWU (Fig. 20, left). The tool is designed in such a way that the active parts can easily be exchanged according

to the above-mentioned tests. The evaluation of the drawing dies after 25 drawing tests (Fig. 20, right) confirms that the lubricated tests show no visible signs of wear in the highly stressed corner areas. On the other hand, the unlubricated tests showed signs of adhesion in these areas. Here, the extent of adhesive wear without coating is significantly increased compared to the reference coating. In addition, typical smoothing marks in the flange area at the level of the corner radius are visible. These are caused by the tangentially acting compressive stresses in the sheet material, with the resulting material thickening and increase of the local surface pressure in this zone.

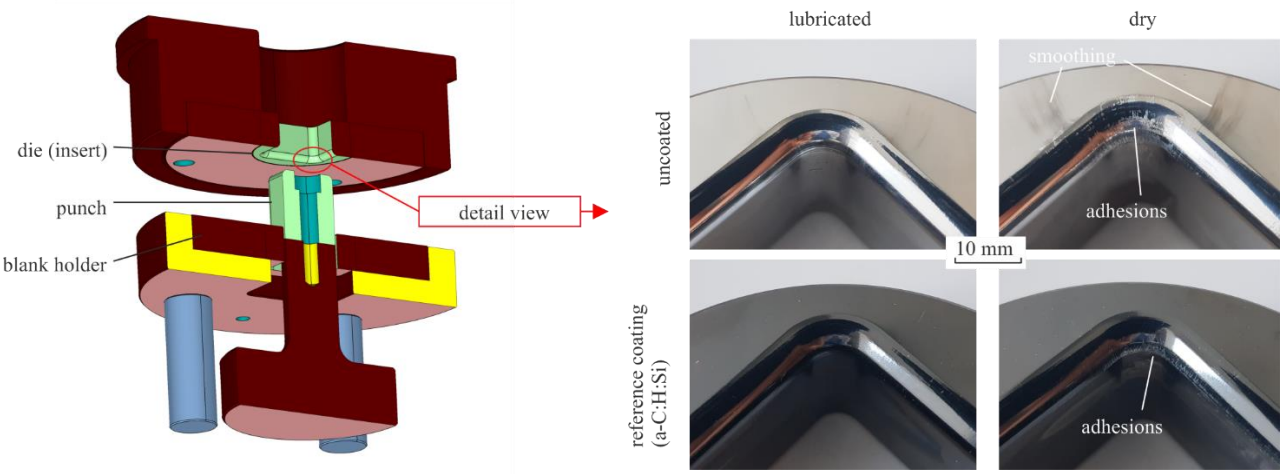

Fig. 20: CAD model of the cupping test tool (left) and detailed views of the die inserts after 25 drawn parts (right)

The maximum achievable drawing depths for all investigated variants were approx. 22 mm and are thus slightly above the values from the FE simulation in Fig. 12. The visual analysis of the sheet surface of the drawn parts in Fig. 21 shows after 25 drawn parts without lubricant, corresponding to the wear patterns of the drawing dies (Fig. 20, right), strong abrasive wear marks in the corner areas. This strong scoring is mainly caused by the formation of adhesions on the die surface. During the drawing tests with lubricant, only smoothing of the sheet surface in the area of the entry radius can be detected. These smoothing marks occur mainly in the flange area due to the tool-bound suppression of wrinkle formation and the associated local increase in surface pressure. It can be assumed that with an increasing number of tests, the depth of the drawn part decreases in the non-lubricated tests, due to greatly increased frictional forces as a result of abrasive and adhesive wear. The effect of the coating on the wear behavior is negligible.

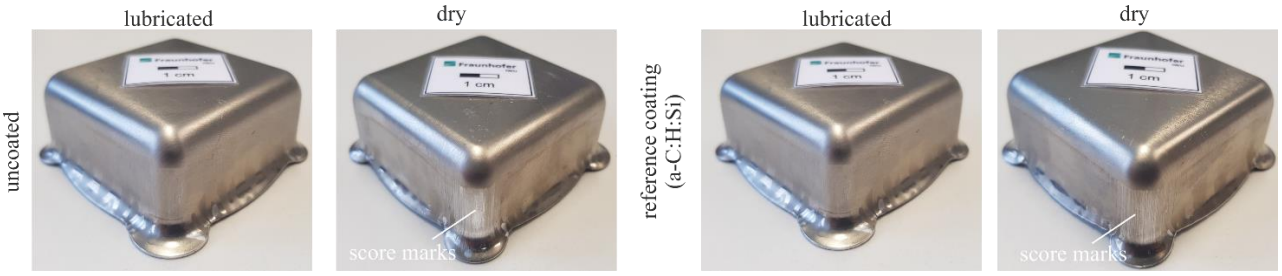

Fig. 21: Visual inspection of the part quality after 25 drawing tests

This confirms the results from the basic experiments. Without the use of lubricants, progressive wear of an adhesive nature on the tool and an abrasive nature on the drawn part occurs with increasing drawing travel. With the high production volumes in the real tool, this wear would lead to scoring or cracking of the component or to total failure of the forming tool. For industrial processes, therefore, unlubricated forming, even using a state-of-the-art DLC coating, is not recommended.

Microstructuring of tribologically loaded functional surfaces

On the basis of a literature research in microstructuring of forming tools, the required properties of the structuring were determined bilaterally between Fraunhofer IWU and the Professorship Micromanufacturing Technology. According to [22], the main factors influencing solid state friction in unlubricated systems are the true contact area between the sliding surfaces, the type and strength of the bond at the interfaces, and the shear

and fracture behavior of the material in or around the contact area. The true contact area between two friction partners is smaller than the apparent or projected contact area due to the multi-scale roughness of technical surfaces and proportional to the normal force [23]. According to the adhesion theory [24], the increase in the true contact surface also increases the frictional power and thus the coefficient of sliding friction [25].

These theories justify the approach of the project to realize a friction reduction by reducing the true contact area with the help of a microstructuring of the tool active surfaces [26]. For this purpose, rotationally symmetric form elements (calottes) were selected, which were placed in different numbers on the active part surfaces and thus allow for a variation of the contact ratio of the tool surface. The real contact ratio is calculated from the difference between the active part surface and the projected surface of the calottes with a diameter of D = 0.6 mm. Three different contact ratios were examined: 100 % (unstructured), 87.5 % and 75 %. As a pattern for the arrangement of the calottes, a grid parallel to the drawing direction and one with an offset of 45° were determined to avoid a preferred direction. To reduce the bearing area to 75 %, the calottes were arranged with a grid spacing of 1 mm, which corresponds to a total of 960 calottes on an area of 1,080 mm². For the realization of a macroscopic bearing ratio of 87.5 % the distance was 1.5 mm (480 calottes).

Flat strip drawing tools:

The calottes were produced by micromilling at the Professorship Micromanufacturing Technology. In a first step, it was investigated to what extent the edge design of the calottes influences the coefficient of sliding friction or the adhesion component. Thus, calottes with a run-in radius (0.1 mm) were milled using coated cemented carbide ball-end cutters with a diameter of D_{Tool} = 0.8 mm (Fig. 22) and tested in strip drawing with flat tools.

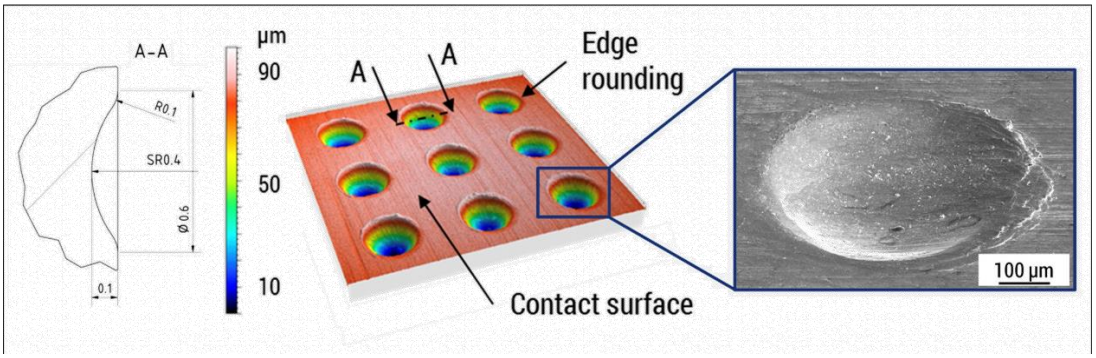

Fig. 22: Various views of the calottes with run-in radius: technical sectional drawing (left), 3D microscopy of the 90° grid on the active part surface (middle) and SEM image (right) of a single calotte

Strip drawing tools with deflection:

For the strip drawing tools with deflection, the calottes were milled with a revised machining strategy: instead of 2.5D milling strategy like for the flat drawing tools, where unfavorable tool engagement conditions are caused by "cutting above the tool center" with v_c = 0 m/min, the calottes were produced by means of 5-axis simultaneous milling. This guaranteed significantly more favorable engagement conditions for the tools, as the cutting was mainly carried out on the largest circumference of the spherical head milling cutter. However, the machining time increased considerably due to this strategy. In addition, due to the wear on the coated cemented carbide cutters of the flat strip drawing tools, cutting tools with CBN inserts were used, which had a significantly longer tool life. Another problem in the microstructuring of the deflected drawing tools was the accuracy of the manufacturing condition. Geometrical deviations within the deflection radius of up to 50 µm could be measured. This prevented the use of a continuous CAM program for the manufacturing of all calottes. Thus, it was only possible to manufacture one row (co-)axially to the deflection radius, since the next row had to be re-measured and manually adjusted with regard to the exact zero plane. Furthermore, delamination phenomena of the DLC coating in the calotte ground were found to be a continuous deficit, Fig. 23. It is assumed that this is due to both increased burr formation on the ground of the calotte and comparatively higher compressive stresses within the coating in this area.

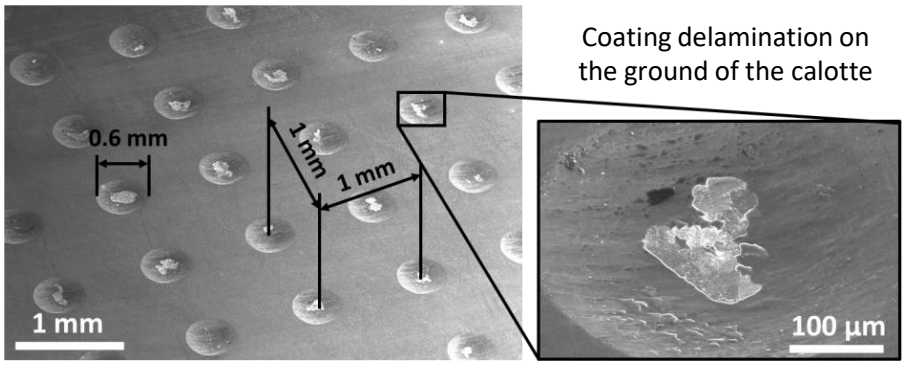

Fig. 23: SEM images of the microstructured functional surface with 75 % macroscopic contact area and chipping of the DLC coating in the ground of a calotte

Oscillating ball on plate test

Fig. 24 shows the coefficient of friction (COF) progressions up to 5 hours and 33 minutes of testing which corresponds to 10^5 cycles. The steady state COF curves were further subdivided into the areas start (0 h to 0.5 h) middle (2.5 h to 3.0 h) and end (5.0 h to 5.5 h), see Fig. 25. The highest COF by sliding against aluminum exhibits the steel specimen (curve 1) which remains nearly in a constant range around 0.62. The COF of the CVDD-coating (curve 2) decreases linearly from 0.42 to 0.36 during the entire test period. The COF of the a-C:H-coating (curve 3) starts at 0.17 and drops after 24,000 cycles to 0.11. The overall noise of the COF curves for the a-C:H and pCVDD-coatings (curve 4) are much smaller than for the other tribological systems, which may be due to less adhesion of the aluminum counter material. The pCVDD-coating exhibits a nearly constant COF of about 0.12 against aluminum during the whole test duration. The diagram confirms a constant COF behavior of the pCVDD-coating.

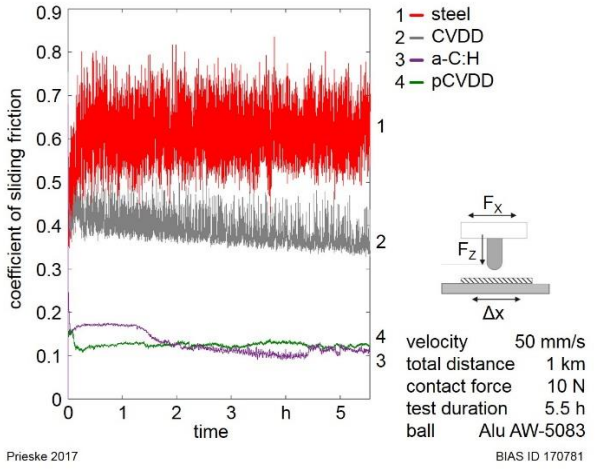

Fig. 24: COF for the different specimens against a round-ended aluminum pin as a function of time, over 5 hours and 33 minutes (about 10^5 cycles)

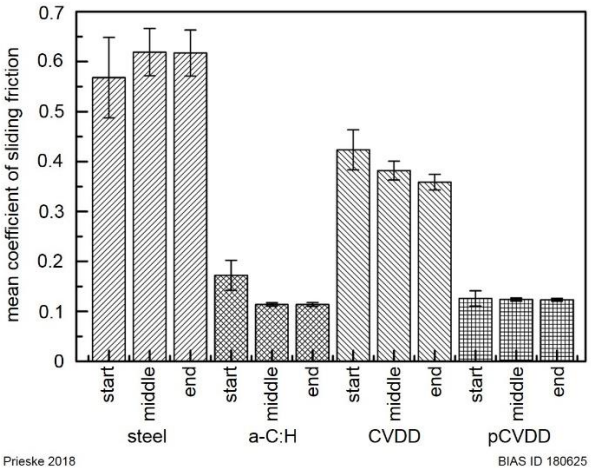

Fig. 25: Arithmetic average of the steady-state sliding COF for the tested systems at the start (0 h to 0.5 h), middle (2.5 h to 3.0 h) and end of the test (5.0 h to 5.5 h).

Fig. 26 presents the measured wear rates of the round-ended aluminum pin in logarithmic scale against the different uncoated and coated test specimens. The highest wear rate of $6 \cdot 10^{-3}$ mm^3/Nm occurred against the CVDD-coating and the smallest wear rate of $4 \cdot 10^{-9}$ mm^3/Nm was observed against the pCVDD-coating. In both cases the dominant wear mechanism was abrasion. The wear rate against uncoated steel is $5 \cdot 10^{-5}$ mm^3/Nm, which is significantly higher compared to that for the a-C:H and pCVDD coated specimens. Iron has been detected at the wear scar of the round-ended aluminum pin by EDX measurements indicating that abrasive and adhesive wear mechanisms took place, as shown in Fig. 28. Tungsten has been detected at the wear scar of the round-ended aluminum pin after testing against the a-C:H coated specimen, as shown in Fig. 30, indicating that the tungsten free a-C:H top layer was worn by abrasive wear. As soon as the tungsten containing layer is exposed, adhesive wear mechanisms occurred which is shown by the transfer of tungsten from the coating to the round-ended pin. The wear rate against the a-C:H-coating is small with $9 \cdot 10^{-9}$ mm^3/Nm. Fig. 27 illustrates the measured wear rates determined from the topography of the wear tracks on uncoated and coated test plates.

The CVDD coated test plate showed material gain due to a transfer from the aluminum pin indicating a negative wear rate. Therefore, the bar for the CVDD coated plate in Fig. 27 is marked by a '+'-sign. The other coated and uncoated test plates all showed material loss indicating positive wear rates. The highest (negative) wear rate showed the CVDD-coated plate which shows a good correlation to the highest aluminum pin wear rate in Fig. 26. The wear rate of the uncoated steel plate is about $6 \cdot 10^{-6}$ mm^3/Nm caused by abrasive and adhesive wear. The lowest wear rates showed the a-C:H coated plate ($9 \cdot 10^{-8}$ mm^3/Nm) and the pCVDD coated plate ($1 \cdot 10^{-8}$ mm^3/Nm). The dominant wear mechanism is abrasion since no noteworthy adhesion phenomena could be proved by EDX analyses.

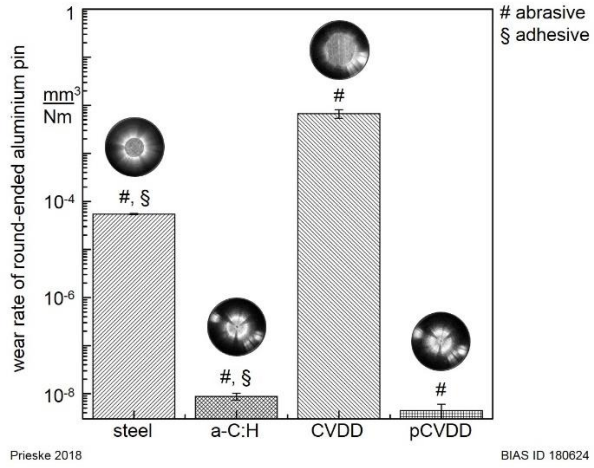

Fig. 26: Wear rate in logarithmic scale of the round-ended aluminum pin after dry tribological testing, including the corresponding wear scar images.

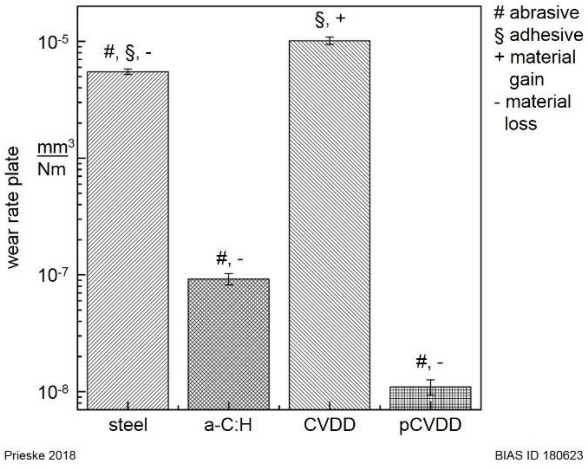

Fig. 27: Wear rates in logarithmic scale of the flat plates after dry tribological testing.

The wear tracks and wear scars were also examined more in detail by SEM/EDX analyses. Fig. 28 shows the results for the uncoated steel plate (a, b) and the corresponding aluminum pin (c). The vertical double arrow represents the alternating sliding direction of the round-ended pin. The resulting width of the wear track is about 3.3 mm at the uncoated steel substrate, see Fig. 28 a). The EDX-mapping (in track center: area 600 µm times 800 µm) in the wear track of Fig. 28 b) proves aluminum adhesion phenomena of about 10 at.-% coming from the round-ended pin. These adhesions are finely distributed throughout the entire wear track. Also, a material transfer from the steel plate to the aluminum pin occurred as determined by the EDX Fe-signals at the wear scar as shown in Fig. 28 c). Narrow wear tracks with widths of about 300 µm are determined at the a-C:H-coating system after dry tribological testing as shown in Fig. 29 a). An EDX-mapping on the area of Fig. 29 b) confirms that the a-C:H:W intermediate layer has been exposed by abrasion, due to reduced C amounts of 78 at.-% and increased W amounts of 11 at.-% and Cr amounts of 9 at.-%, after 10^5 cycles. The exposure was also confirmed by a comparison of the micro Raman spectra inside and outside of the wear tracks. Increased chromium signals in the EDX mapping indicate that also small areas of the Cr/CrN_x interlayer were exposed. An EDX-mapping of the wear scar at the round-ended aluminum pin shows adhesion of tungsten and carbon, see Fig. 29 c). However, it can be assumed that a friction reducing transfer film has been formed on the counter body (compare with Fig. 24). The signals of carbon, tungsten and oxygen could also be an explanation of the drop of COF partially below the pCVDD-coating after approximately 1.5 hours of testing.

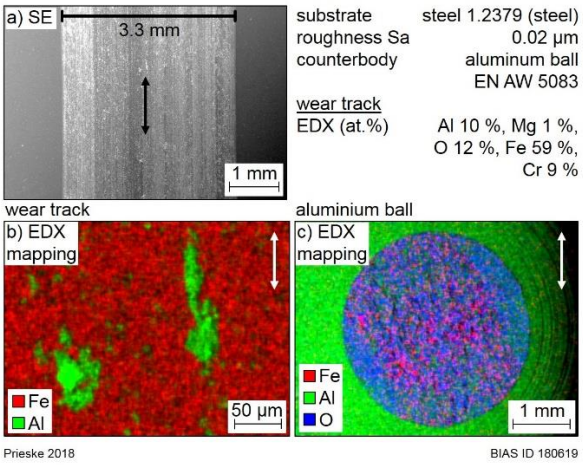

Fig. 28: a) Representative SE image of a wear track of the uncoated steel plate after ball-on-plate testing using a round-ended aluminum pin and EDX-mappings of b) the wear track and c) the wear scar.

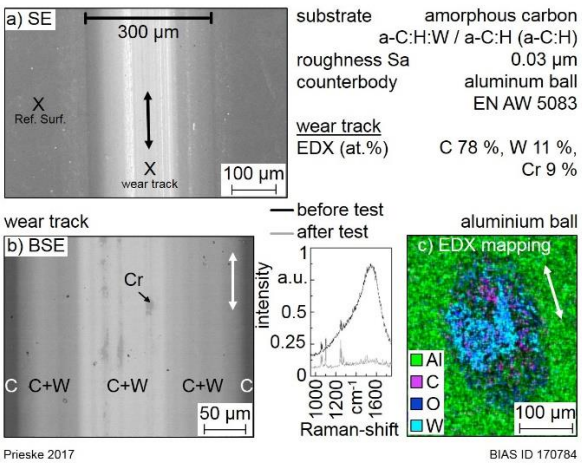

Fig. 29: a) Representative SE image of a wear track on the a-C:H-coating after ball-on-plate testing using a round-ended aluminum pin, b) BSE image of the wear track including Raman spectroscopy and c) EDX-mappings of the wear scar.

Fig. 30 a) shows the SE image of a wear track on the tested pCVDD-coating. The average width is about 300 µm and therefore the same as on the a-C:H-coating (compare with Fig. 29). The BSE image in Fig. 30 b) and the EDX analysis confirms that no aluminum or other elements from the counter material alloy adhered on the pCVDD-coating. The first-order diamond Raman line is detected at 1,339 cm^{-1} before and after tribological testing, which proves the existence of diamond and no change in the residual stress of the coating, due to the fact that a rise in the residual stress leads to a shift of the peak towards higher values. Comparing the Raman spectra before and after the test an increase of the G peak at 1560 cm^{-1} [27] takes place, which indicates a rise of the graphitic amount. At the wear scar of the round-ended aluminum pin signals of carbon were detected by means of EDX analyses, see Fig. 30 c). These carbon signals can be explained by the formation of a transfer film which transferred to the counter material as already mentioned for the a-C:H-coating. The origin surface roughness Sa of the pCVDD-coating was 14 nm. The dry tribological test led to an increase of the roughness at the wear track to Sa 21 nm. The resulting wear rate is about one order of magnitude lower than of the a-C:H-coating resulting in a much lower mean track depth of 0.1 µm compared to 1.1 µm. The wear tracks micro- and nano-topography was studied more in detail by means of AFM. Fig. 31 a) illustrates an overview image of the pCVDD-coating after dry testing recorded by laser scanning microscopy. An AFM measurement with the field size of 15 µm x 15 µm was recorded in the center of the wear track. Wear grooves in microscopic scale parallel to the sliding direction of the round-ended aluminum pin have formed as can be seen in the measured profile of the AFM image in Fig. 31 c) as well as in Fig. 31 a). Compared to the results of Podgursky et al. [28] no ripple formation in the wear scar is detected.

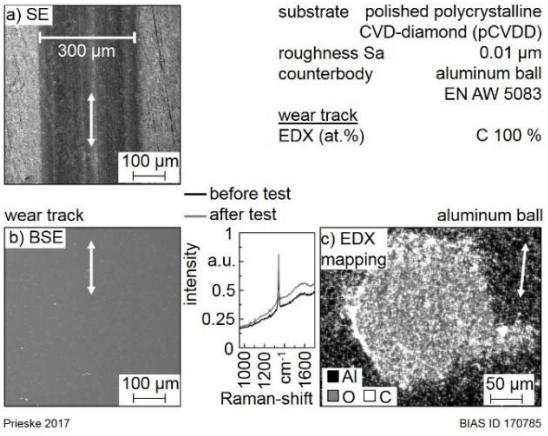

Fig. 30: a) Representative SE image of a wear track of the pCVDD-coating after ball-on-plate testing using a round-ended aluminum pin, b) BSE image of the wear track with corresponding Raman spectroscopy measurement at and besides the wear track and c) EDX mapping of wear scar of the round-ended aluminum pin.

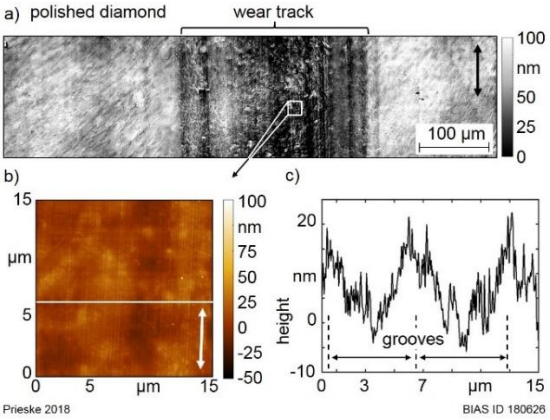

Fig. 31: a) Wear track of the pCVDD-coating determined by laser scanning microscopy as overview and b) AFM image in the middle of the wear track with c) corresponding roughness profile located at the white line.

Post-processing of CVD diamond coatings

According to Tsigkourakos et al. [29] the resistance of an undoped CVD diamond layer is greater than 10 GΩ. The resistance of the diamond layers deposited by the LaPlas CVD process is greater than the maximum measurable resistance of the Fluke 117 multimeter of 60 MΩ (cf. Fig. 35). In order to enable a smoothing of the diamond layer by electrical discharge machining, the extent to which the resistance of the diamond layer can be reduced by the introduction of foreign atoms was investigated. In the LaPlas CVD process, aluminum oxide and silicon carbide rods were used as solid precursors, which were vaporized in situ for the introduction of foreign atoms. The use of boron, which is the most frequently used element in chamber-based processes to introduce electrical conductivity into diamond, was not used in this atmospheric process due to its harmfulness to health. In order to ensure a constant introduction of foreign matter into the diamond layer, the intensity of the respective peaks in the emission spectrum was kept constant by adjusting the feed rate of the precursor. The diamond layers, which were deposited with aluminum oxide rods evaporated in situ, resulted in a delamination of the diamond layer in the fringe area of the coated surface. On the remaining diamond-coated surface no change of the resistance could be measured, and the spectrum of the photoluminescence measurement is identical to that of an undoped diamond layer.

An increasing in situ evaporation of silicon carbide rods leads to a decreasing area, which is deposited by a CVD diamond coating, as shown in Fig. 32. A reduction in electrical resistance can be measured using a multimeter. This is distributed inhomogeneously on the surface of the diamond layer as shown in Fig. 33 (top). The resistance increases from the outside to the inside and lies in the middle of the coating above 60 MΩ. The increased presence of silicon in the edge area of the coating can be explained by the lateral feed of the precursors into the plasma flame. At the Fraunhofer ISC (Würzburg), a layer resistance of 2.53 MΩ ± 1.29 MΩ could be measured on the surface of a single diamond crystal using the van der Pauw 4-point measuring method, Fig. 33.

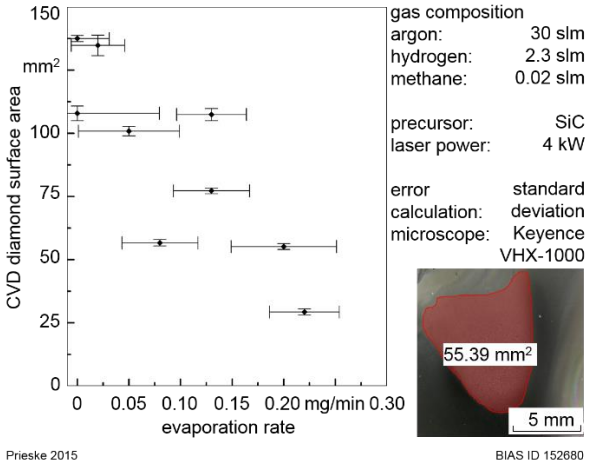

Fig. 32: Coating area of the diamond layer as a function of the evaporation rate of the SiC precursor.

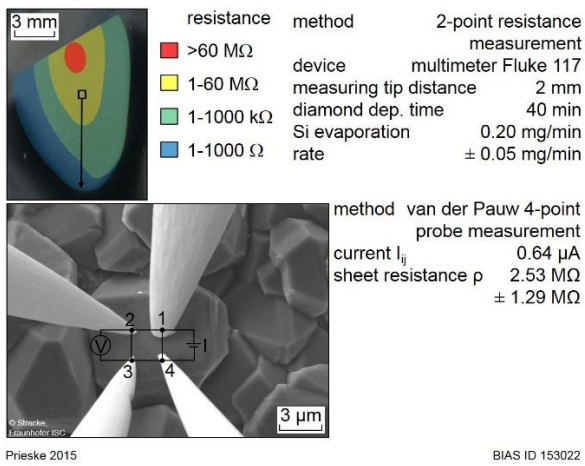

Fig. 33: Distribution of the electrical resistance over the coating surface (top) and measurement of the coating resistance on a single diamond crystal (bottom).

To achieve a more homogenous distribution of the reduced electrical resistance and thereby ensure an overall machineability of the silicon doped CVD diamond coating by electrical discharge machining, a nozzle was attached to the exit point of the plasma flame. ANSYS flow simulations were performed to assess the influence of different nozzle geometries. Six different nozzle geometries were simulated, with the result that the geometry shown in Fig. 34 a) results in the plasma flame with the most symmetrical shape. The result in Fig. 35 c) shows that the use of the nozzle enables the deposition of diamond layers which have an electrical resistance of the same order of magnitude on the entire layer surface.

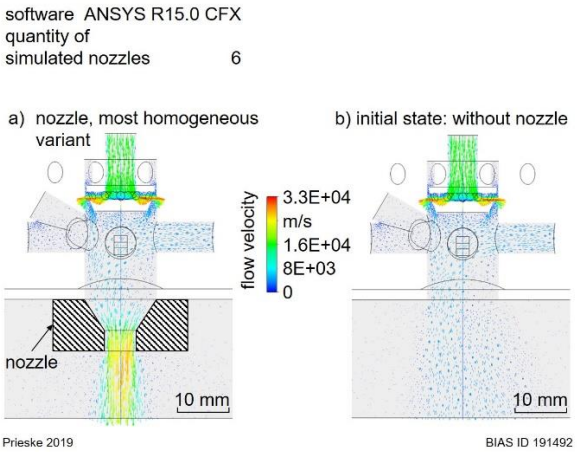

Fig. 34: Result of the flow simulations regarding the influence of different nozzles on the plasma flame, a) nozzle geometry leading to the most homogeneous flame and b) initial condition without nozzle.

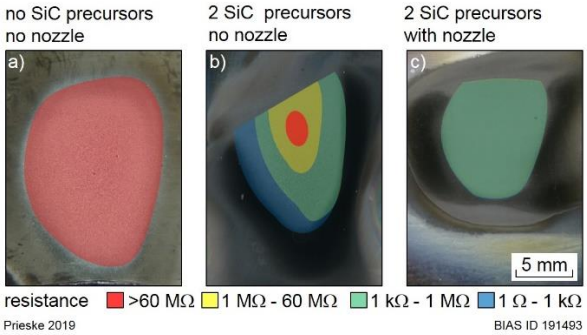

Fig. 35: Distribution of the electrical resistance of an a) undoped and a doped sample b) without and c) respectively using a nozzle.

Fig. 36 shows a comparison of the photoluminescence spectrum with and without incorporated silicon. The broad band luminescence of diamond in the range between 500 nm and 650 nm is much more intense with the diamond layer with incorporated silicon than with the pure CVD diamond layer. At 738 nm, an intense peak is measured at the diamond layer with incorporated silicon. This peak is characteristic for silicon defects (SiV centers) in diamond [30] and thus proves the incorporation of individual silicon atoms into the crystal lattice of the diamond. In combination with the resistance measurements, this leads to the conclusion that a supply of silicon into the laser-induced plasma leads to a reduction of the electrical resistance of the diamond layer, not only through silicon clusters located between the diamond crystals, but also through a doping of the crystal lattice. The use of a nozzle leads to a homogeneous introduction of silicon accompanied by a homogenous electrical resistance on the surface of the silicon doped CVD diamond film.

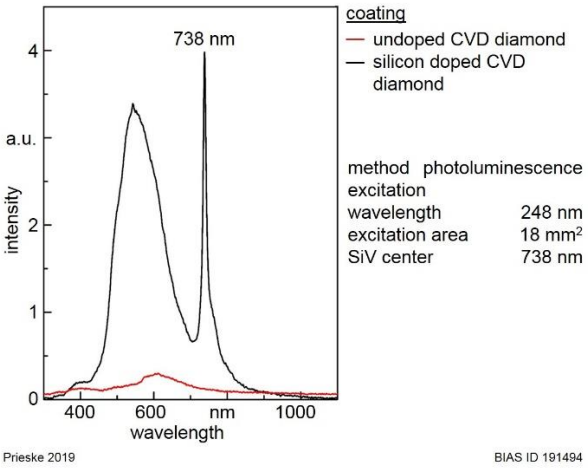

Fig. 36: Photoluminescence measurement on a pure and a silicon doped diamond layer.

Electrical discharge machining of CVDD

The characterization of the silicon doped CVDD layers was necessary before the experimental investigations. At this time, there have been no publications and known research projects dealing with micro electrical discharge machining of silicon doped diamond layers. The thickness of the deposited layers by the LaPlas-CVD process were about 10 µm to 12 µm and the electrical resistance was in the range of several kiloohms to 1 MΩ. Thus, a sufficiently high electrical conductivity was guaranteed.

Microstructuring by EDM

At the beginning the principle electrical discharge machining of doped CVDD layers was proven and then the machinability of the diamond layer substrate was characterized. Due to the challenge of producing doped CVD-diamond layers on steel substrates, for the characterization of the EDM process molybdenum substrates coated with silicon doped diamond as well as commercial boron doped diamond materials were used. For this purpose, experiments were conducted under variation of open-circuit voltage, discharge power level and tool polarity. Fig. 37 shows an overview of the micro bore arrays machined with varying open-circuit voltages and both positive and negative polarity, captured with the laser scanning microscope Keyence VK-9700.

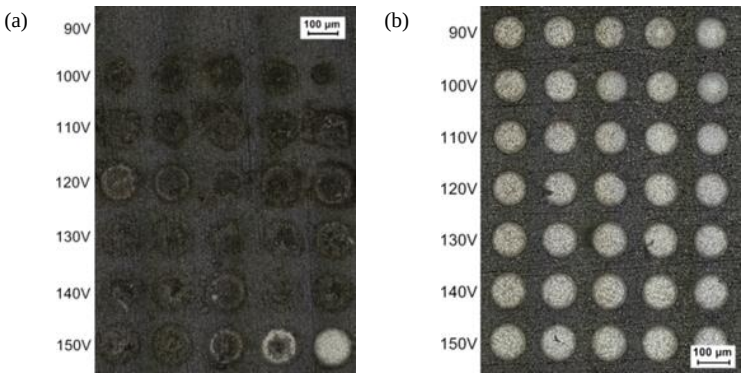

Fig. 37: Microscope images of micro holes for positive and negative tool polarity, machined with varied open circuit voltage and constant discharge energy level (CF102) with negative tool polarity (a) and positive tool polarity (b)

The microscope images clarify the qualitative differences of the EDM results as a function of the tool polarity. The lighter areas in the bottom of the micro holes identify the molybdenum substrate material. Fig. 37 (b) shows the machining results for varied open-circuit voltages and positive tool polarity. No reproducible removal results were achieved. With an electrode feed step of 50 µm only irreproducible removal depths of 0 µm to 2.7 µm were achieved. Solely at 150 V a significant removal of the diamond layer was achieved for two experiments. However, the removal was so high, that the 10 µm to 12 µm thick layer was removed completely. The micro bores shown in Fig. 37 (a) were machined with negative tool polarity. For all experiments clearly defined ablations were achieved. Constant diameters for each open-circuit voltage indicated good reproducibility. Fig. 38 shows SEM micrographs of the micro holes with 900x and 2000x magnification.

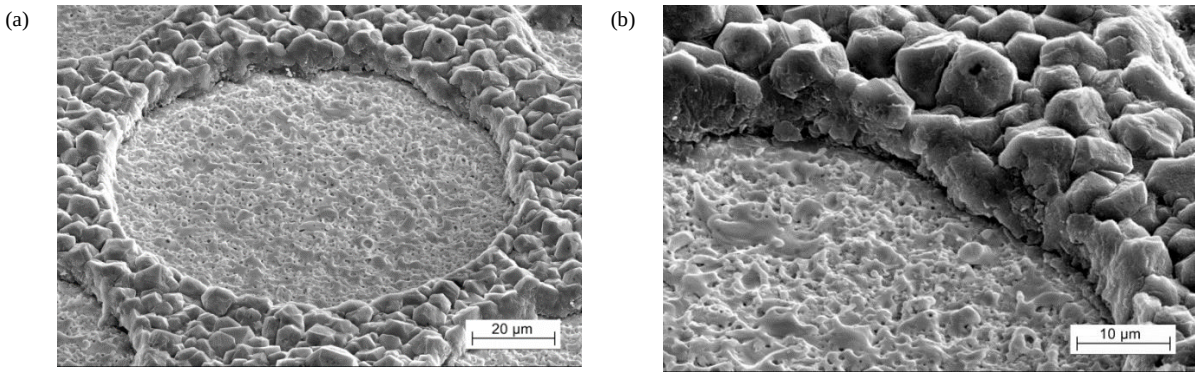

Fig. 38: SEM micropgraphs of micro holes, machined at 150V, CF102 and positive polarity with 900x (a) and 2000x magnification (b)

The shown micro hole has a diameter of 93 µm and a depth of 10 µm. Furthermore, it is clearly visible that the diamond layer was completely removed. This was confirmed by an EDX analysis in which 61.8 % molybdenum and 38.2 % carbon were detected. The fraction of carbon is related to the used hydro carbonaceous dielectric.

With increasing open-circuit voltage, a tendential increase of the achieved removal depths was observed. As the open-circuit voltage increases, the diameter also increases. This is related to an increasing spark gap at increasing open-circuit voltages. Similar to the experiments with variable open circuit voltage, the discharge energy level was varied from CF100 to CF105 at a constant open circuit voltage of 150 V and positive tool polarity. A clear correlation between width and depth of the eroded micro bores could not be validated.

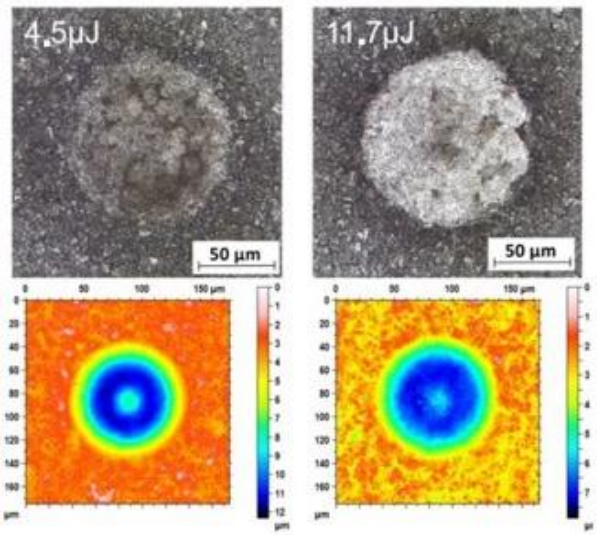

Fig. 39: Microscope and false colour images of micro holes of boron doped CVD diamond layer, machined with negative polarity, 100 V open-circuit voltage and 4.5 µJ or 11.7 µJ discharge energy

The application of a positive tool polarity results in a complete removal of the diamond layer. By adapting the process parameters with negative polarity, micro bores could be reproducibly machined without layer damage. Due to electrode wear the bores resemble the shape of a calotte. The average depths of the micro bores were in the range of 4 µm to 8 µm. Fig. 39 shows microscope images and false colour images of two micro bores in a 12 µm thick boron doped CVDD layer from DiaCCon. These two bores were machined with negative tool polarity, 100 V open-circuit voltage and a discharge energy of 4.5 µJ or 11.7 µJ, respectively.

In addition to the qualitative removal result, the material removal rate and the wear rate were also analysed. Significant differences were found depending on the tool polarity. With the micro-EDM typical negative tool polarity, a maximum removal rate of 7.4×10^{-4} mm³/min was achieved at 120 V and CF100. This corresponds to about 5 % of a typical removal rate of steel under the same conditions. The reason for this is the significantly lower electrical conductivity of the material. With positive tool polarity, removal rates, which were nearly increased by a factor of 10 could be achieved. The removal rate at 120 V and CF102 was 0.139 mm³/min. Experiments at 60 V showed good reproducibility. For higher open-circuit voltages (120 V, 160 V) in combination with discharge energy levels from CF104 and higher, the thermal stress on the electrode was too high, resulting in damage and excessive electrode wear. With a negative polarity, the increase in open-circuit voltage and discharge level tends to result in a higher tool wear rate. The determined tool wear rates were 10 times greater than the removal rate (minimum 6.2×10^{-4} mm³/min at 60 V and CF100). By contrast, the maximum wear rate with positive tool polarity is only 1.4×10^{-4} mm³/min at 60 V and CF102. This special removal and wear behaviour with a low material removal and wear rate for negative polarity and a high material removal rate with simultaneously low wear rate for boron doped materials was also described by Iwai et al. [31] for so called “meso-EDM” processing.

EDM - Smoothing

Fig. 40 shows a comparison of the unprocessed surface and the surfaces machined with a discharge energy of 2.6 µJ for both doping materials. Further, a summary of the roughness characteristics depending on the discharge energy is shown.

(a)

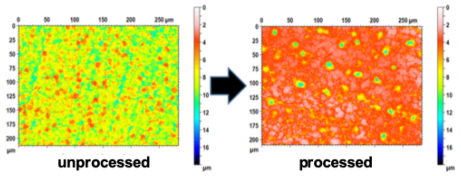

Parameters	Sa [µm]	Sk [µm]	Spk [µm]	Svk [µm]
unprocessed	1.43	4.59	1.97	1.29
2.6 µJ	0.47	1.20	0.69	1.26
6.9 µJ	0.59	1.47	0.48	1.63
13.7 µJ	0.71	1.99	0.80	1.36

(b)

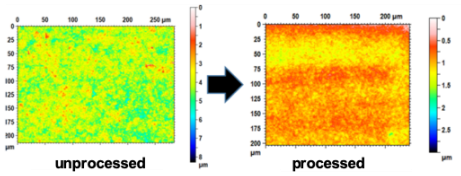

Parameters	Sa [µm]	Sk [µm]	Spk [µm]	Svk [µm]
unprocessed	0.37	1.14	0.62	0.38
2.6 µJ	0.10	0.33	0.17	0.11
6.9 µJ	0.18	0.59	0.26	0.22
13.7 µJ	0.20	0.64	0.25	0.27
18.1 µL	0.21	0.64	0.39	0.27

Fig. 40: Comparison of machined and unmachined surfaces based on false colour images and roughness measurements of silicon (a) and boron (b) doped CVD diamond

The roughness parameters decrease with decreasing discharge energy for both doped materials and that the lowest roughness was achieved with the lowest discharge energy of 2.6 µJ. This smoothing can be seen in the false color images. Based on the Fig. 40 (a), it becomes clear that the machined surface has a pitted structure. This is related to silicon clusters, which were evaporated in the EDM process and thus influencing the roughness characteristics negatively. Fig. 41 shows a SEM micrograph of the silicon doped diamond layer in unmachined and machined state. The unprocessed surface illustrated in Fig. 41 (a) shows a sharp-edged character of the individual diamonds (Sa = 1.43 µm). The machined surface in Fig. 41 (b) shows a significant gradation and smoothing of the surface (Sa = 0.83 µm). The graphitization of diamond above a temperature of 750 °C is described in the literature [32, 33, 34, 35] as a main erosion mechanism of diamond. The diamond layer smoothed by EDM was examined by Raman-spectroscopy. A peak at 1332 cm^{-1} was found after the process, which proves the presence of diamond.

(a)

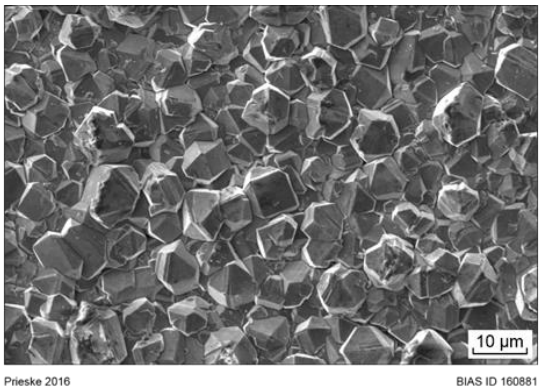

(b)

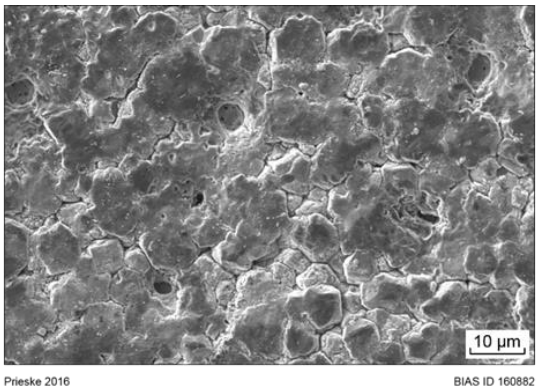

Fig.41: SEM micrographs of unprocessed (a) and silicon doped CVD diamond layer smoothed by EDM (b; 130 V, CF100 = 2.6 µJ, negative polarity)

Furthermore, boron doped CVDD erosion experiments were performed at constant open-circuit voltage (60 V) and discharge energy (4.3 µJ = CF102), varied tool polarity and path coverage varied from 0 % to 50 %. The Fig. 42 shows false color illustrations of the generated surfaces for both cases.

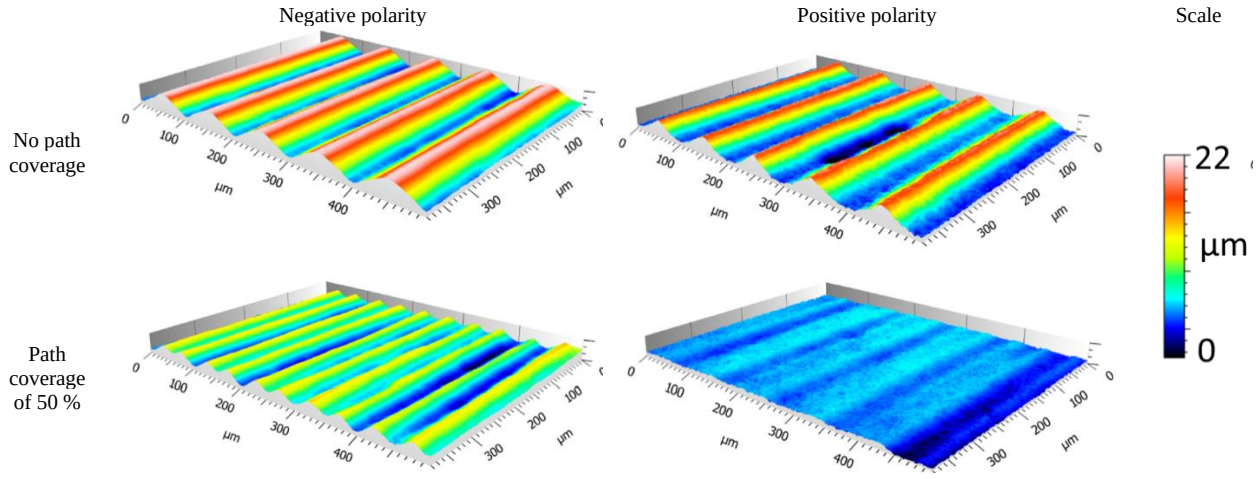

Fig.42: 3-D false color illustration of boron doped CVD diamond material after the EDM path process as a function of path coverage and tool polarity

Translational roughness was generated for both polarities. At 0 % path coverage a roughness Rz of approx. 21.5 µm were determined, irrespective of the tool polarity. This translational roughness decreases with increasing path coverage factor. At 50 % path coverage and negative polarity a translational roughness of approx. 11 µm was determined. For the same path coverage, a stronger smoothing effect was observed for positive polarity, so that a translational roughness of approx. 3.5 µm were achieved. For optimum machining of doped diamond layers, positive tool polarity in combination with low voltages and low discharge energies of negative tool polarity is preferable. The reasons are the better reproducibility of the removal results, the overall higher removal rate with adjustable small tool wear and stronger smoothing effects. Overall, it is shown that the approach of surface smoothing and microstructuring with electrodes with a diameter of only 90 µm is possible, but not expedient for the planned application on large-area forming tools.

Substrate pre-treatment of steel for subsequent CVDD coating

The pre-structuring of substrate surfaces to ensure a technologically relevant adhesive strength of thin and thick layers applied to them is state of the art in many known applications, such as the mechanical roughening of cylinder linings for coating with iron-based functional layers. In the addressed application of CVDD on the steel X153CrMoV12-1, microstructuring of the surface is intended to ensure coating adhesion for a technological load. The aim is to exploit both effects to increase the coating adhesion (mechanical interlocking and surface enlargement to increase potential growing points) and to reduce layer-inherent residual stresses. Methods for increasing surface roughness with stochastic distribution are afflicted with various negative side effects, e.g. for corundum blasting: residuals remain in the surface. Furthermore, the predictability of the processing result is comparatively low. For this reason, a defined microstructuring by machining processes was selected. In this regard it is important that a deterministic surface roughness can be predicted, modified and generated reproducibly. In addition, the extended goal included the production of large-area active tool parts, mostly with 3D free-form surfaces, which is why machining processes using CAM software are favored. There are multiple studies, which examine the impact of the substrate surface microstructure on the adhesion strength of CVDD coatings with different substrate materials.

Substrate pre-treatment by cutting processes

Face milling was initially selected as machining method for the steel surfaces. For this purpose, the formation of the kinematic roughness, which is typical for milling processes, was investigated by using coated cemented carbide end mills and steel specimen in a hardened state (50 HRC + 2 HRC). Analogously, experimental investigations with grinding tools were carried out. In addition, a surface simulation tool was developed which outputs the ideal kinematic roughness as a high-resolution point cloud. This simulation tool for the prediction of the surface microstructure should reduce the experimental scope. Following the initial findings, simulative and subsequently experimental work was carried out with ultrasonic vibration superimposed milling for the microstructuring of the steel surfaces.

Kinematic simulation model

The kinematic simulation model for calculating the surface microstructure produced by machining processes with geometrically defined cutting edges was developed in MATLAB. A virtual 2D or 3D tool as a point cloud

of all relevant geometrical elements is intersected along a given trajectory with the likewise virtual workpiece. This is volumetrically represented as a dexel model. To describe the entire body volume, each beam element in a matrix is assigned an exact X- or Y-position in two-dimensional space in discrete form. The advantage of this form of spatial discretization is that due to the two-dimensional, equally spaced point distribution, the memory requirement for the volumetric model increases only to the second power, but at the same time the model can be resolved much higher in the Z-direction, since an increase in accuracy of the height values has no influence on the memory utilization. The kinematic simulation is a discrete procedure in which the movement is not represented continuously but in discrete time steps. In order to be able to represent the process realistically despite this simplification, a correspondingly high temporal resolution is necessary. In addition, the simulation tool was extended in the course of the project so that, in addition to the 2D tool paths, 3D tool paths, e.g. in ultrasonic vibration superimposed milling, can be displayed and observation with and without re-cutting of the structures is possible. Furthermore, the implementation of real measured 3D tools is possible [36, 37, 38].

Milling without UVAM

During the investigations on the characteristics of the kinematic roughness as well as the influence of the machining parameters on selected surface parameters, some correlations could be determined - especially the feed plays the most dominant role. In addition, the path overlap also has a relevant significance for the preferred direction of the surface finish. The selection of measuring field size and position can significantly influence the surface parameters.

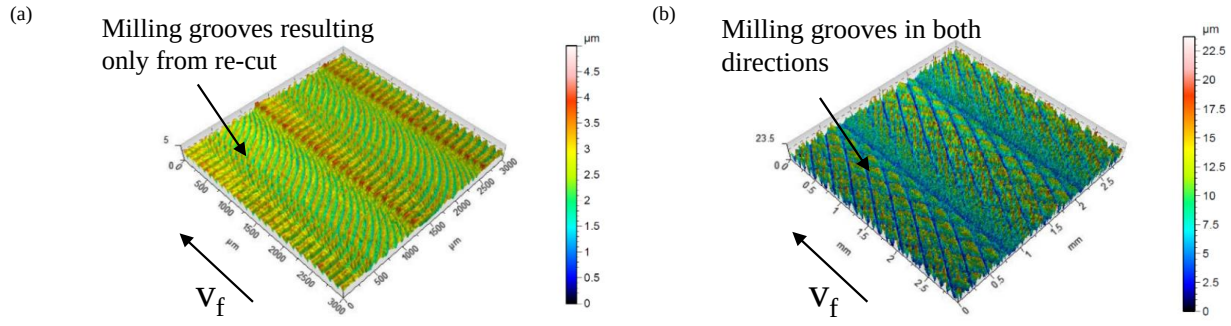

Fig.43: Visual comparison of face milled (a) and simulated (b) surface with DTool = 3 mm, fz = 0.06 mm, ae = 1.3 mm

Fig. 43 gives a visual comparison of a milled surface (a) with a simulated surface (b), by using the same machining parameters. This graphic evaluation already shows that during the simulation of face milling under ideal process conditions certain geometric characteristics occur periodically and repeatedly. In reality, however, the milling process and thus the final surface microstructure is additionally influenced by other factors, such as tool wear, machine vibrations and material properties. When looking at a milled surface, the milling grooves of the tool cutting edges become clearly visible. It is noticeable that the revolving cutting corner creates the dominant part of the surface microstructure by cutting the kinematic microstructure resulting from the preceding intervention of the cutting corner again. Analytical calculations as well as experimental studies on the targeted influencing of this "re-cutting effect" were then carried out. Thereby, the characteristic traces appeared irregularly and independently of the considered parameter constellation. Therefore, no correlation between the formation of the re-cutting effect and the feed, depth of cut or the wear condition of the tool cutting edge, respectively, could be found. According to this, this effect offers further research potential if it is to be used specifically to influence the microstructure.

To get more information about the roughness compensating properties of the diamond coating, the possibility of transferring the kinematic roughness to molybdenum samples was investigated. This did not require an intermediate layer for CVDD coating. Different parameter sets with a clear formation of the kinematic roughness were selected and transferred to molybdenum sheets with geometrically analogous experimental tools. During the subsequent surface analysis, it was found that, in contrast to machining of the hardened steel, the kinematic roughness was strongly superimposed. This sub roughness is probably due to the plastic deformation properties of molybdenum. During the subsequent coating process, closed as well as adhesive CVDD with a layer thickness of approx. 20 µm could be deposited. However, the characteristic machining marks on the substrate surface remained clearly visible afterwards, Fig. 44. Therefore, no roughness

compensating properties can be shown for this thickness range and morphology (crystallinity: approx. 5 µm – 20 µm in maximum) of the CVDD coating. However, no statement could be derived from these results regarding the challenges of coating steel materials, such as the different coefficients of thermal expansion of steel and diamond.

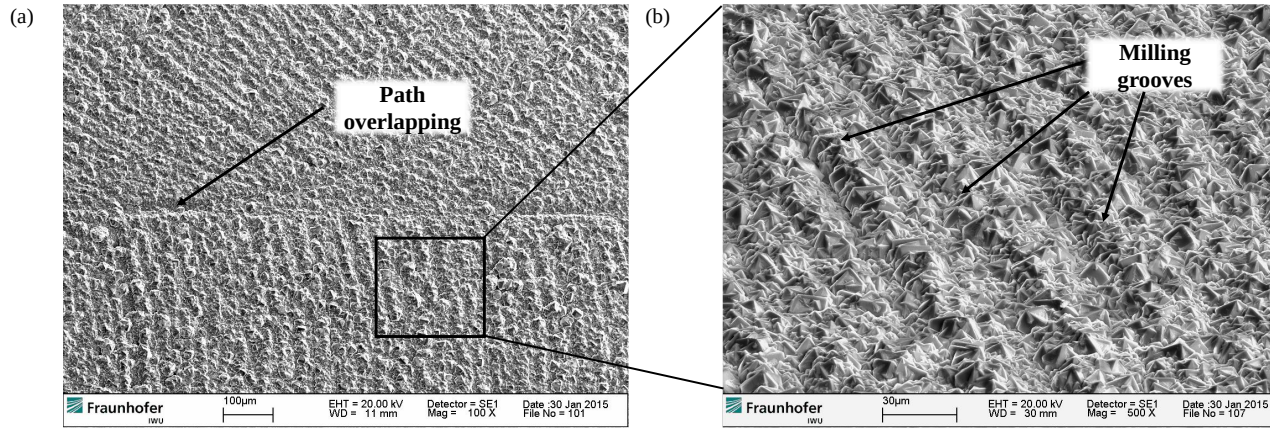

Fig.44: SEM micrographs of CVDD coating on by face milling microstructured molybdenum with 100x (a) and 500x (b) magnification

Grinding

Analogous to the microstructuring of steel by milling, face grinding was considered as a further process. CBN grinding pins in two different grit sizes (B126 and B64) were used. In initial preliminary tests, the wear development of the tools was recorded, and a decision was made for using cooling lubricant. The use of cooling lubricant emulsion was therefore possible because no micro-crack formation occurred due to a quenching effect and no amorphous surface layers were formed by rapid melting and cooling of the machined steel substrate.

During the surface analysis after the main tests carried out, it was found that in the overlapping areas material throw-ups are formed in the feed direction. Due to their characteristics they make the quantitative evaluation of the surface with the relevant surface parameters more difficult. The mean arithmetic height with significantly lower values than 1 µm does not indicate a significant increase in the effective surface area. The maximum reached surface increase (Sdr) was therefore only above 1 %. The behavior of the surface microstructure with respect to the preferred direction was also considered. It was found that a strong anisotropy in the feed direction is created due to the material throw-up. Further preferred directions were not detected across the tests.

Repeat tests were carried out to investigate the extent to which the results of the tests performed are reproducible. The differences were partly considerable, mainly due to increasing tool wear on the face and edge of the grinding pins. It can therefore be assumed that the process used does not appear to be suitable with regard to the reproducibility of certain surface structures and surface parameters or that there is a large variation in the work results. Furthermore, there is no interrupted cut for most of the grains on the flat surface of the tool. Rather, the grains are permanently engaged, depending on the position of the tool on the surface. Derived from these findings, surface treatment for a defined increase in roughness by grinding is not recommended.

Ultrasonic vibration assisted milling – UVAM

From the tests carried out, some findings could be derived, both in terms of machining technology and with regard to the first coating results. The surface and layer analyses of the test samples coated with LaPlas-CVD diamond showed that the isotropy of the surface microstructure in particular has a great influence on the layer adhesion, since stress peaks occur along dominant preferred directions (such as overlapping areas and feed or grinding grooves), which lead to layer delamination. In addition, thicker layers than the (average) profile height of the substrate structuring should be aimed for, since CVDD coatings with a layer thickness in the single-digit or low two-digit micrometer range do not have roughness compensating properties. In order to take advantage of mechanisms of mechanical clamping and stress reduction within the layers, microstructures without a preferred direction should be produced, whereby the profile height should be at most half the desired layer thickness of approx. 20 µm. For this reason, the investigations focused on vibration-superimposed milling in

the ultrasonic range. It is characterized by the fact that the conventional tool path (cycloid) is superimposed with an additional effective movement in the direction of the tool axis, which can be described mathematically by a sine function. It is possible to generate an isotropic structure distribution, a determined profile height and a predefined structure distance by an adaptation of the process parameters.

There are only a few research results with respect to milling, especially face milling, with ultrasonic vibration assistance according to Lauwers et al. [39]. The complexity of the superimposed motion as a function of the required workpiece surface is one of the main reasons. However, the superposition of vibrations in the direction of the tool axis during milling has an influence on surface structure formation and is described for example from Maurotto and Wickramarachchi [40]. The results of the investigations show that a change in the surface roughness can be achieved by a variation of the machining parameters as well as the vibration parameters. Furthermore, they concluded that due to the tool wear it is necessary to develop tools as well as coatings for the application of (ultrasonic) vibration assisted milling processes. Kuruc et al. demonstrated the dependence of the surface roughness on the ratio between a constant ultrasonic frequency and the spindle speed in a micro milling process of an aluminum alloy [41]. Different superposition effects (interferences) can occur which have a high influence on the surface characteristics and cannot be fully explained yet. In addition, experimental investigations using a multi-edged milling tool were carried out. They further intensified such effects by using cutting geometries which differ from each other. It is shown that vibration assisted machining processes enable the generation of predefined surface microstructures. However, due to its complex kinematics, the application of previous process simulation is required.

Initial performance tests were carried out with standard tools and specimens made of X153CrMoV12-1 in the soft annealed condition (255 HB). Double-edged, coated cemented carbide end mills (D_{Tool} = 5 mm) were used. By means of the ratio of a (fixed) measured vibration frequency of the system and the rotational speed of the tools, the distance between the structures along the tool circumference can be calculated and thus defined. From this, both the cutting speed and the feed can be defined. In all cases considered, the feed was chosen analogous to the structure distance in order to obtain the highest possible isotropy. The results of the surface and tool wear analysis provided several insights:

- An offset (along the tool axis) of the cutting-edge corners of multi-edged tools in the micrometer range, is transferred to the surface microstructure and has a clear influence on the structural characteristics and the isotropy.
- In particular the tools flank face, but also the minor cutting edge, come into contact with the previously generated microstructure with unfavorable cutting parameters, so that it is deformed.
- The above-mentioned effect causes increased tool wear in the form of chipping or breakouts, especially on the cutting edge, at points with alternating mechanical load.

Based on the machining parameters, the oscillation parameters and the tool geometry – especially the relevant part of the tool tip – four different simulation models were created, Fig. 45. By lining up individual cycloids in the feed direction, it is possible to set a defined offset of the sinusoidal structure after each rotation. Since there are both fluctuations within the spindle speed and the resonant frequency in the real machining process, a clear ratio of these variables cannot be predicted. In the most cases it is not an integer, which results in a slight misalignment. In the simulation, therefore, the two "extreme cases" are compared: no offset ("valley follows valley", (a) and (c)) and maximum offset half a structural distance ("valley follows peak", (b) and (d)), below named without and with displacement. Furthermore, both variants were simulated with ((c) and (d)) and without the re-cutting effect ((a) and (b)) of the rotating cutting corner. For the surfaces without re-cut, a path shorter than the tool diameter was simulated. The resulting surfaces from the simulation are shown in Fig. 45 exemplarily for the experimental parameters of *UVAM 3.6 100*, Tab. 5.

Tab. 5: Experimental plan and machining parameters

#	A_P	f_z (≈ λ)	v_c	Contact*
UVAM 3.6 100	1.8 µm	100 µm	120 m/min	no
UVAM 3.6 50		50 µm	60 m/min	yes
UVAM 6.6 100	3.3 µm	100 µm	120 m/min	yes

*Contact between flank face and microstructure due to the parameter ratio of the clearance angle to the wavelength and the amplitude

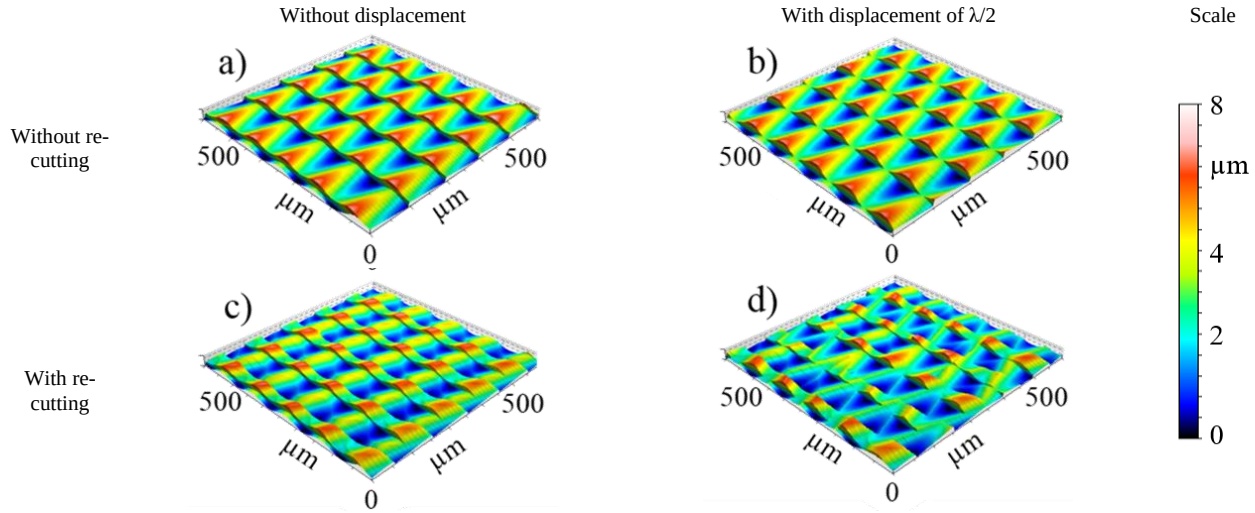

Fig.45: Simulated surfaces as a variation of the reference microstructure *UVAM 3.6 100*

Fig. 46 shows some results of the manufacturing of the microstructures from Tab. 5. It should be noted that the *UVAM 3.6 100_II* (a) was produced with a double-edged tool, while the remaining three combinations were produced with single-edged cutters. In (b) the different surface profiles of sections are shown in both the feed direction (kinematic roughness) and the cutting direction (sinusoidal profile). In (c) and (d), the actually produced surfaces are compared with the simulated surfaces of the parameter combination of *UVAM 3.6 100* on the one hand optically and on the other hand by means of their Abbott and material proportion curves. (c), as with all surfaces under (a), are specimen in the soft annealed condition, while (d) represent the microstructured surface resulting from manufacturing of a hardened specimen. It can be clearly seen that the microstructure of the softer specimen is more similar to that of the simulation without a re-cut, while the microstructure of the hardened specimen is more similar to the simulation with a re-cut. This is possibly due to the different material behavior of the workpiece material. The results presented in detail under [37].

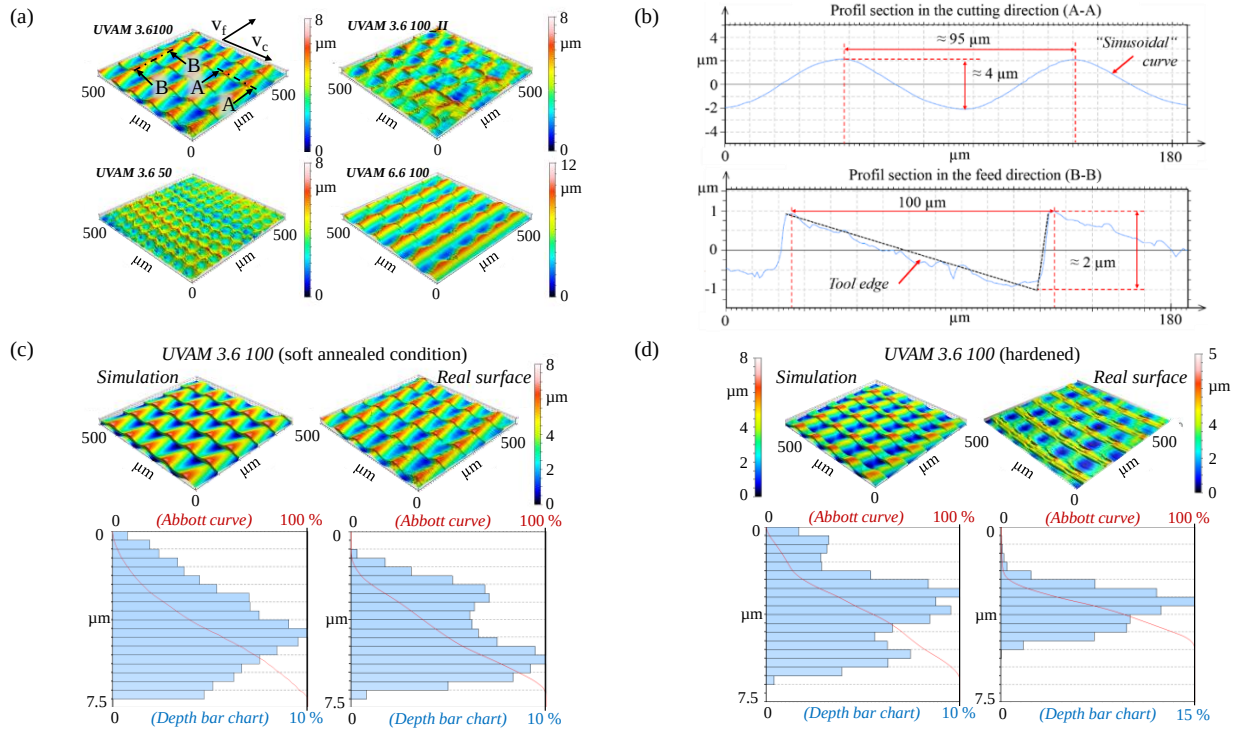

Fig. 46: Results of the surface microstructure analysis

In Fig. 47, the shown condition (above, left) is representative for all new tools. It can be seen that the tool without a contact of the flank face and the microstructure (*UVAM 3.6 100*) have nearly unworn cutting edges

and cutting corners. Only a very small rounding could be determined, which can be attributed to a successive wear of the coating. However, the wear of the tools of test *UVAM 3.6 50* and *UVAM 6.6 100* is clearly conspicuous. Larger edge sections at the minor cutting edge as well as the rake face are broken off, and the coating in this area is spalled. This is attributable to the unfavorable engagement conditions during the machining process, where the hammering contact between the minor flank face and the microstructure resulted in high mechanical stresses at the cutting edge and the tool tip. Those vibrations ultimately led to the local failure of the coating and the substrate material and consequently to a rapid increase of the tool wear. The wear analysis of the tools used for the microstructuring of the hardened specimens confirmed the results of the surface analysis: in particular the minor cutting edge as well as the cutting corner showed considerable chippings. Thus, the chipping of the cutting edge increased and led to a higher deviation from the simulated microstructure in comparison with machining in the soft annealed state. The main wear type is abrasion. In addition, large areas of delamination of the coating on the rake face could be determined. It can be concluded that the coating or its adhesive strength is not suitable for the hard machining with regard to the mechanical load. The slightest wear occurred at the tool used for *UVAM 3.6 50*, where the feed per tooth and also the cutting speed were lower.

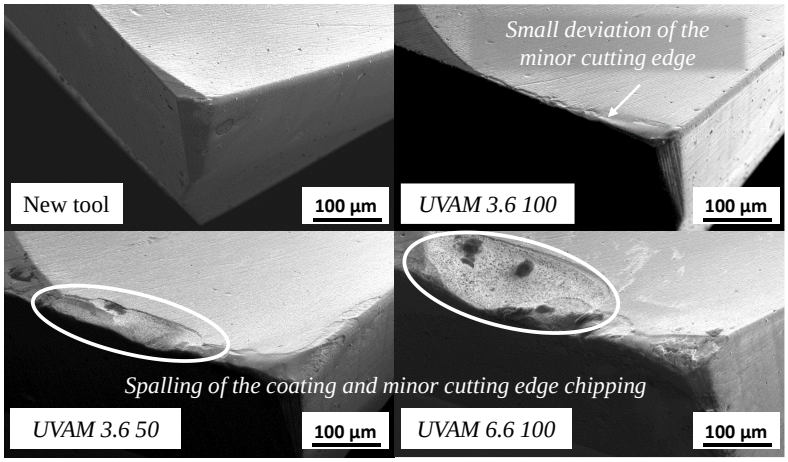

Fig. 47: Wear analysis of the single-edged tools with characteristic signs of wear for favourable (*UVAM 3.6 100*) and unfavourable cutting conditions (*UVAM 3.6 50* and *UVAM 6.6 100*)

As a result of these first findings of the UVAM process, the boundary conditions were changed: The process parameters were adapted in such a way that a collision between the flank face and the secondary cutting edge with the calculated surface microstructure was excluded using the standard tools; in addition, these were used with a single cutting edge to exclude a height offset of the individual paths. The cutting edge had a defined rounding of (approx.) 5 µm. A high degree of agreement between the manufactured and simulated surfaces could be achieved continuously. However, the structural clearances were still in areas that did not correspond to those of the preliminary considerations (e. g. $A_{US} \approx 5$ µm and $\lambda = 100$ µm ≙ aspect ratio of 1/20), due to the orientation of the process parameters on the tool geometry. Therefore, special tools with modified geometry considering the relevant cutting part and an adoption to the desired structural dimensions were procured. In addition to the definition of the clearance angle (15°) and the angle of the minor cutting edge (15°), also the corner was varied: nearly sharp, rounded ($r_b = 5$ µm) and chamfered). However, it merged that both the relatively large corner radius and the chamfer had a very dominant influence on the microstructure compared to the dimension of the microstructure, resulting in strong preferred directions of the surface. The nearly sharp corner, in turn, was not very wear-resistant and tended to break out quickly.

To prevent the relatively high tool wear, tools with analogous cutting-edge geometries made of cubic boron nitride (CBN) were used. For selected parameter combinations and specimens made of the steel X153CrMoV12-1 in both the soft annealed and hardened condition, these tools were tested. However, no improvement in the wear behavior and thus the reproducibility of the microstructures could be achieved, as the tools broke off almost on first contact. This is due to the comparatively higher brittleness of the CBN cutting material in comparison to cemented carbide tools and the comparatively much higher alternating mechanical load caused by the ultrasonic vibration.

For the last investigations, a maximum aspect ratio of approx. 1:4 of the surface microstructure was aimed for. This was realized by amplitudes A_{US} of 4.5 µm and 6.5 µm, which correspond to structural distances of 18 µm

and 26 µm, respectively. In addition, the larger structural distances were combined with the smaller amplitude to get a third microstructure with roughness characteristics between the two extremes [38]. Because of the high aspect ratio, tools with a clearance angle of about 40° were necessary. Thus, to ensure the stability of the cutting edge, they had a negative rake angle of -10°. The angle of the minor cutting edge was 15° and to protect the sharp cutting corner, they had a very small chamfer (approx. 14 µm x 60° to the major cutting edge).

In the visual comparison of the UVAM microstructured surfaces with the previously simulated, it was found that the milled surfaces correspond to those simulated without re-cutting. In addition, a slight displacement of the microstructure occurs, Fig. 48 (c). This results from a non-controllable, non-integer ratio of the rotational speed and the oscillation frequency. The two variants of the simulation in Fig. 48 show the case without (*SIM_1 6.5 26*) or with a maximum structural displacement (*SIM_2 6.5 26*).

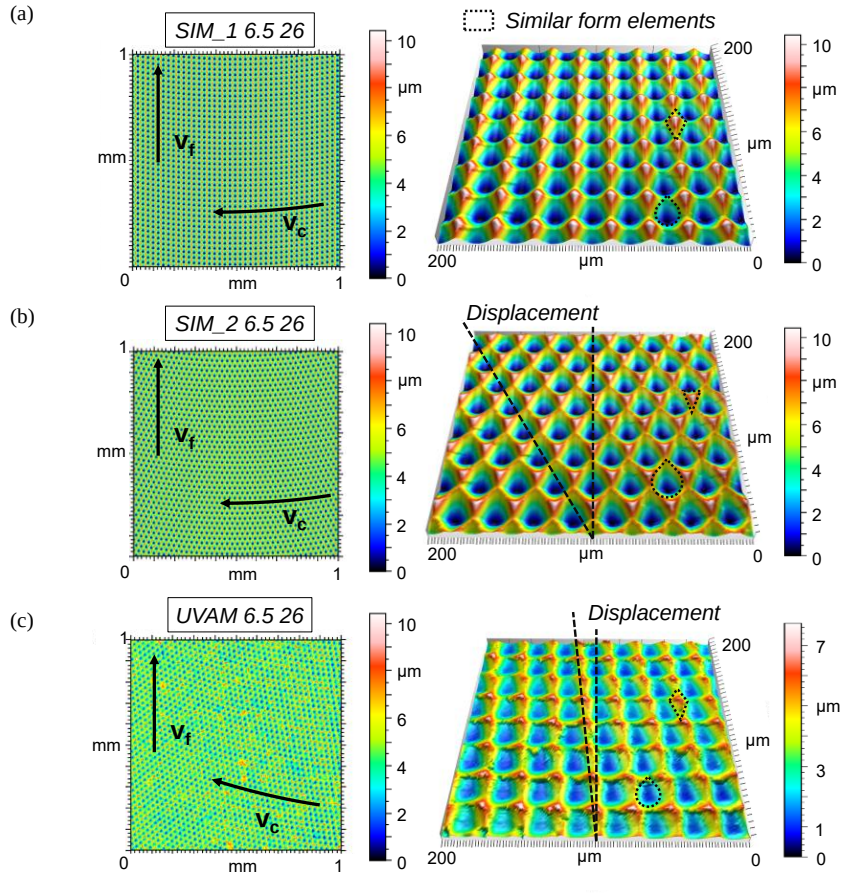

Fig. 48: Visual surface comparison of *SIM_1 6.5 26* (a), *SIM_2 6.5 26* (b) and *UVAM 6.5 26* (c)

Furthermore, it is shown, that the profile height of the generated surface is smaller than the simulated height. This could be due to the damping of the amplitude by the tool engagement. The quantitative comparison of the surface parameters Sa and Sdr confirms the considerations of the surface design, Fig. 49. It could be noted that the smallest value for the arithmetic mean height corresponds with the smallest developed interfacial ratio for the three by UVAM generated surfaces. The highest value for the developed interfacial area ratio of the specimens (*UVAM 6.5 26*) results from the higher amplitude.

Although the qualitative (as well as the quantitative) accordance between the simulated and experimentally manufactured surface microstructure is sufficient, it has to be noted that this only applies for the middle area of the milled path. In the overlapping area, the microstructure is distorted, and this leads to strongly anisotropic areas, Fig. 50. In addition to the microstructure, further elements on the surface, such as burr formation, occur.

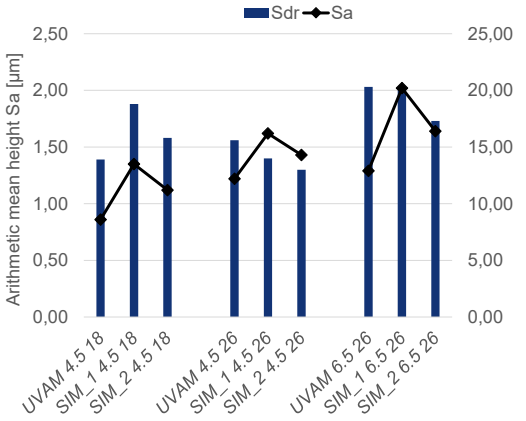

Fig. 49: Results of the analysis of the simulated surfaces and the surfaces generated by UVAM

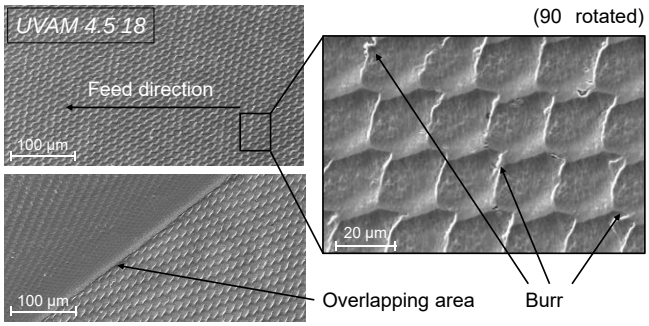

Fig. 50: SEM micrographs of a surface generated with UVAM with regard to burr formation (right) and path overlap (below)

CVD diamond deposition on steel substrates

Due to the carbon diffusion into the steel substrate, an intermediate layer is necessary as a diffusion barrier [42]. The deposition of intermediate layers was investigated using the evaporation of solid rods in the LaPlas system using an argon/hydrogen plasma flame, so that the entire coating system can be deposited in one system. Fig. 51 shows that coatings could be applied using Si_3N_4 and SiC rods. The evaporation of the Si_3N_4 precursors is similar to a plasma spraying process and leads to a porous coating. The materials aluminum and yttrium used as binding agents in the rods can also be detected on the surface. The evaporation process of the SiC precursors leads to a green coloration of the plasma flame and a homogeneous coating. The EDX analysis detects mainly silicon and oxygen on the surface (Fig. 51 right). Fig. 52 shows the growth rate in the border area and in the middle of the silicon carbide-containing coating. The coatings were deposited with the evaporation of two SiC precursors and a substrate surface temperature of 800 °C. In the border area of the coating there is a much smoother coating with a higher growth rate than in the middle of the coated surface. EDX measurements showed 60 wt.% silicon, 34 wt.% oxygen and 5 wt.% carbon in the border area. In the middle of the coating a composition of 49 wt.% silicon, 45 wt.% carbon and 4 wt.% oxygen was detected. This means that oxygen from the ambient air is built into the layer at the edge of the coating and silicon oxide is thus deposited. Silicon carbide is predominantly present in the middle range. This explains the different growth rates. The coating area produced in this way is 40 mm^2 and could be increased by means of a 2-axis cross table. The coating with an increased deposition area was analyzed by X-ray diffraction and a composition of the coating of 69% silicon, 16% silicon dioxide and 15% silicon carbide (alpha SiC) was determined. In the following, the coating is referred to as silicon coating.

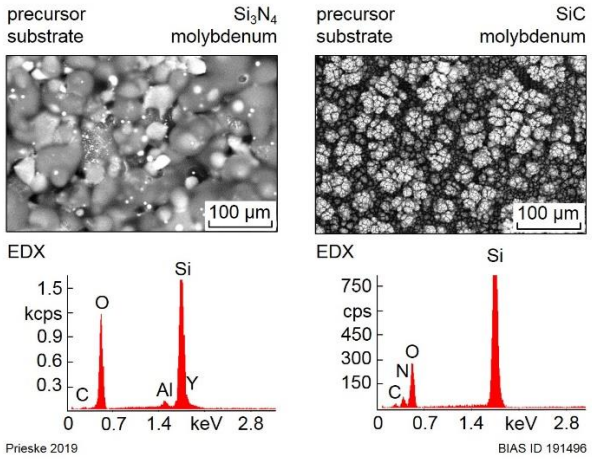

Fig. 51: Surface structure and EDX spectrum of a coating based on vaporized Si3N4 (left) and SiC precursors (right)

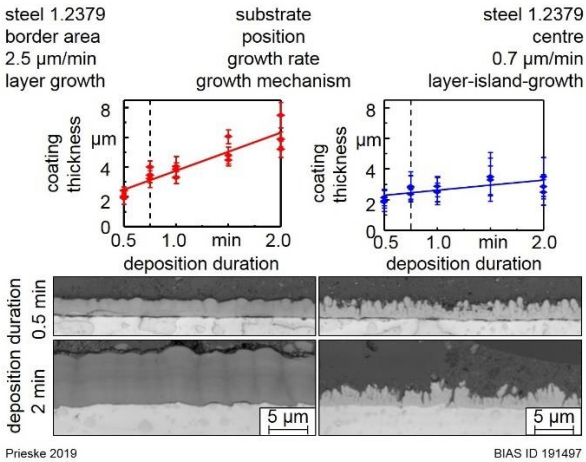

Fig. 52: Growth rate of the silicon coating, in the marginal area (left) and in the middle (right).

The process window of the LaPlas CVD process was investigated by a variation of the methane/hydrogen ratio from 0.15 % to 5.0 % on etched hard metal substrates, which is shown in Fig. 53. The results show that the deposition temperature depends on the methane/hydrogen ratio. It was shown that a CVD diamond deposition

is possible in the temperature range between 650 °C and 1100 °C. In Fig. 54 a 4 µm thick silicon coating was deposited on steel at 800 °C. The coating was applied to the steel at a temperature of 800 °C. A polycrystalline CVD diamond coating was then deposited at a temperature of 1050 °C with a layer thickness of 4 µm. It is shown that a diamond layer can be deposited on the silicon intermediate layer (Fig. 54 b). During the cooling phase after the coating, the diamond layer and partly also the silicon intermediate layer are delaminated (Fig. 54 a) and c). The EDX mapping on a cross section (Fig. 54 d), carried out at the position of Fig. 54 b), questions whether the silicon intermediate layer effectively acts as a diffusion barrier for iron, since iron can be seen inside the silicon layer.

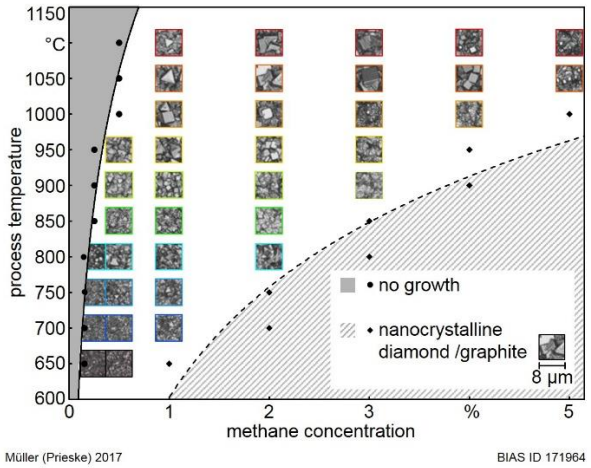

Fig. 53: Possible process temperatures for diamond layer deposition depending on the methane concentration.

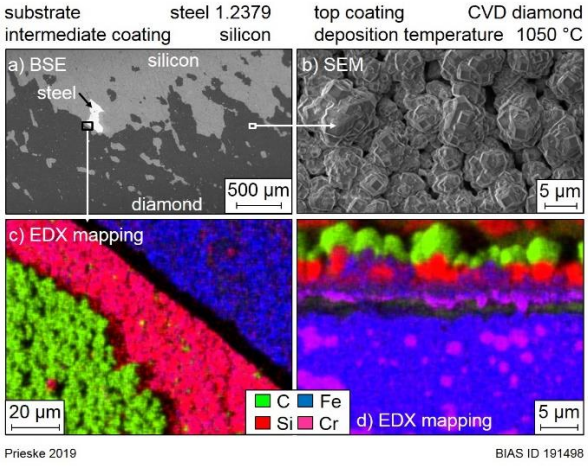

Fig. 54: CVD diamond coating on ground steel with an intermediate silicon layer, a) BSE image of the coating, b) SEM image of the diamond layer and EDX mappings of the c) plan view and d) the cross section at a diamond coated area.

In Fig. 55 differently manufactured microstructures coated by a 2.4 µm thick chromium nitride layer by Oerlikon Balzers are shown as SEM micrographs as well as the measured Sa and Sdr values. Both parameters vary over a wide range from the very smooth polished surface with Sa 0.1 µm and Sdr = 2% to the rough corundum blasted surface with Sa 3.0 µm and Sdr = 297%. In comparison to Fig. 49 the developed interfacial area ratio (Sdr) values increase and the Sa values decrease due to the chromium nitride coating. EDX measurements of the chromium nitride coating detected 47 at.% nitrogen and 53 at.% chromium, which verifies a chromium nitride coating.

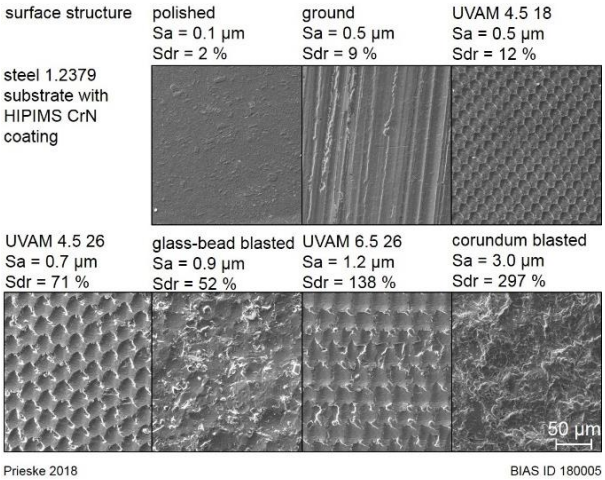

Fig. 55: SEM micrographs of the different microstructures realized on steel substrates and coated by a chromium nitride layer.

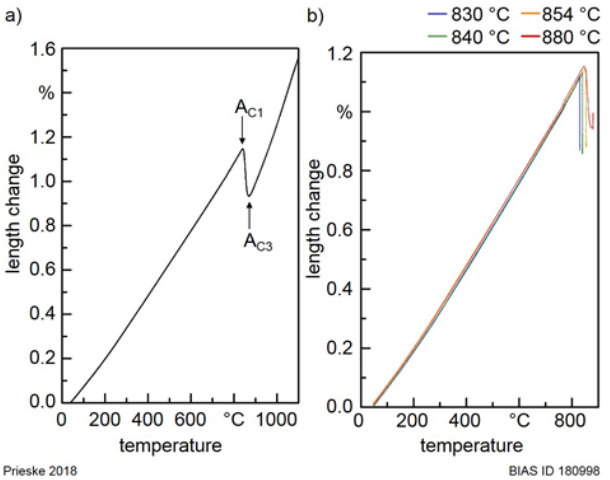

Fig. 56: Dilatometer measurements of X153CrMoV12-1 steel specimen a) with a heating rate of 2 K/s up to 1100 °C and b) with a heating rate of 7 K/s and different holding temperatures for 40 minutes.

The result of the dilatometer measurement shown in Fig. 56 a) with a slow heating rate of 2 K/s shows an austenite to ferrite transformation and thereby a nonlinear change in length. The temperatures of phase transformation A_{C1} and A_{C3} are measured at 840 °C and 871 °C. In Fig. 56 b) the test parameters are adapted to the process conditions, with a heating from room temperature to the deposition temperature in 2.5 minutes

and a subsequent holding time of 40 minutes at the deposition temperature. The tests show that a holding temperature of 840 °C leads to the smallest length change of 0.86%. With the LaPlas CVD process the lowest achievable temperature on steel substrates, where a diamond coating can be deposited, is 700 °C. During the heating process of the dilatometer test the length change at 700 °C shows a length change of 0.93%. Fig. 57 shows the result of the local CVD-diamond deposition at 840 °C with a thickness of 8 µm. In the photography of the coating, the bright grey area is the CrN layer, where the diamond coating delaminated. The dark grey area is the remaining diamond coating. The black box shows the position of the measured height profile. The scale of the height profile in Fig. 57 and Fig. 61 is individually chosen to show the optimum contrast, with the low structures in blue colour and the high structures (usually the diamond coating) in red. The four microstructured specimens with the lowest roughness (Fig. 57 left side) led to a delamination of the diamond coating in form of a diamond foil, so that nearly no diamond is left on the substrate. The glass-bead blasted substrate led to a flake like delamination. The *UVAM 6.5 26* specimen shows that especially in the overlap area with a distorted microstructure a complete delamination occurs. No damages could be observed at the diamond coating on the corundum blasted specimen. A higher magnification of the remaining diamond coatings on the different substrates is shown in Fig. 58. On each image the polycrystalline character of the coating can be seen.

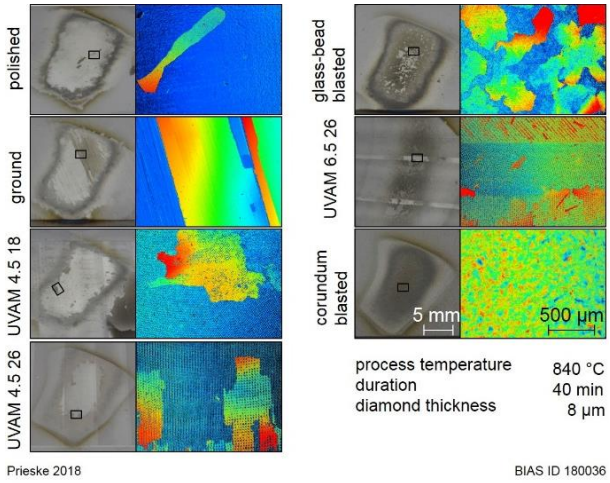

Fig. 57: Photography and height profile of the diamond coating deposited at 840 °C.

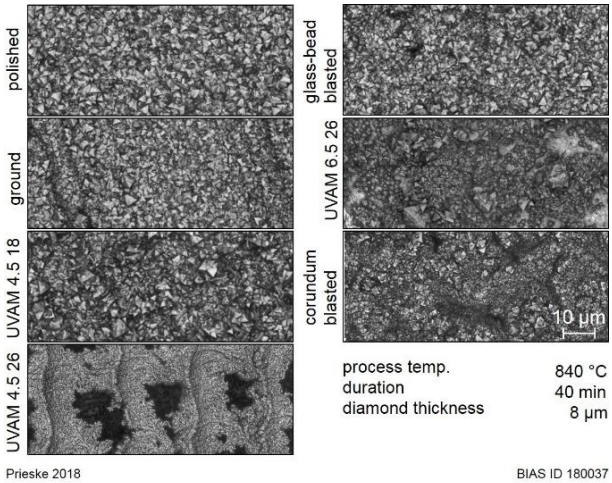

Fig. 58: Microscopic images at high magnification of the diamond coatings deposited at 840 °C, which show the crystalline structure.

The two structured specimens *UVAM 4.5 26* and *UVAM 6.5 26* show that in the valleys of the surface structure the diamond coating is not a closed layer. Especially the higher peak to valley height of specimen *UVAM 6.5 26* leads to the growth of large diamond crystals on the peaks and just small diamond crystals in the valleys, as it is marked in Fig. 59 on the right image. The diamond coating on the corundum blasted substrate has small uncoated or delaminated areas as can be seen in Fig. 60. The white dots in Fig. 60 a) represent the CrN coating, which is not coated by diamond as can be seen in the detailed image in Fig. 60 b) and was verified by an EDX measurement.

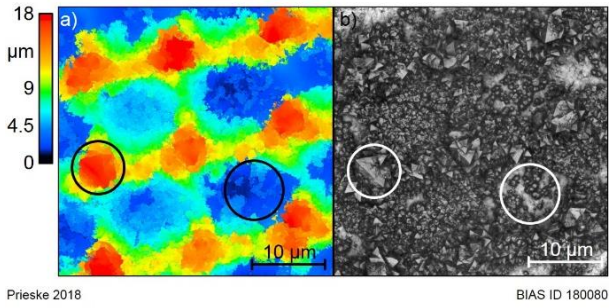

Fig. 59: Diamond coating deposited at 840 °C on an UVAM 6.5 26 substrate a) as a height profile and b) microscope image on the same position.

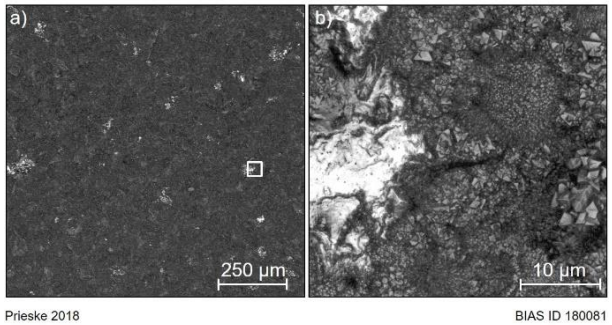

Fig. 60: a) Overview image and b) detailed image (box shown in a) of the diamond coating deposited at 840 °C on corundum blasted substrate.

Fig. 61 shows the result of the local CVD-diamond deposition at 700 °C with a thickness of 2 µm. Compared to the diamond coatings deposited at 840 °C (Fig. 57) the area of delamination decreases. In the height profiles

of all specimen clear delamination can be seen except on the ground and corundum blasted specimen. On the ground substrate a closed diamond layer is deposited with lots of small delaminated areas (black dots in the height profile). The overlap area of the UVAM specimens promotes the delamination of the diamond coating, as can especially be seen in the photography of specimen *UVAM 4.5 18*. The highly magnified images of the diamond coatings deposited at 700 °C in Fig. 62 show a crystalline structure with diamond crystals smaller than 1 µm. Small delaminated or u22ncoated areas can be seen in most images, which have a length smaller than 10 µm.

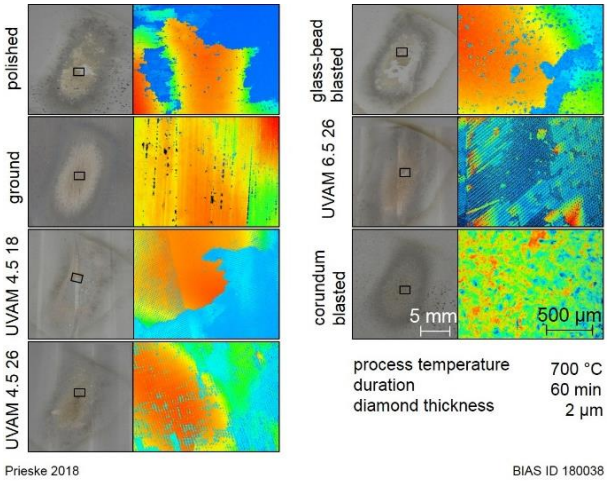

Fig. 61: Photography and height profile of the diamond coating deposited at 700 °C.

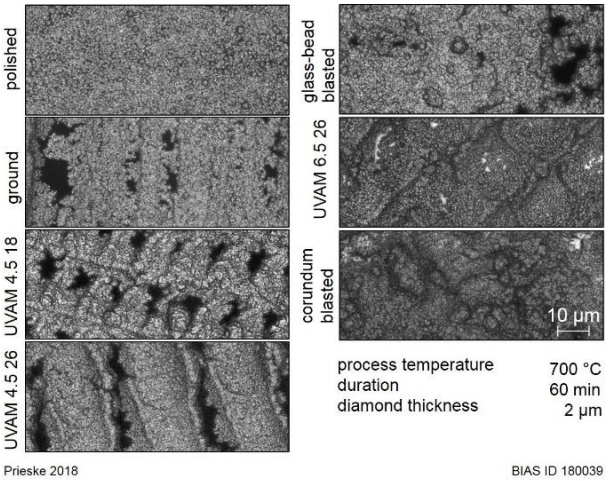

Fig. 62: Laser scanning microscope images at high magnification of the diamond coatings deposited at 700 °C, which show the crystalline structure.

A representative Raman spectrum of a diamond coating deposited at 840 °C and 700 °C is shown in Fig. 63. The spectrum of the coating deposited at 840 °C shows the peak at 1332 cm^{-1}, which proofs residual stress free microcrystalline diamond [16]. No residual stress is measured, because the measurement is done on a diamond coating which is partly delaminated. The peak at 1560 cm^{-1} is the so-called G-peak [43] which shows that the coating also has a graphitic content. The peak at 1190 cm^{-1} can be related to incorporated nitrogen in the diamond coating, which is introduced by the CrN interlayer. Zhang et al. [44] detected an increase of two peaks at 1190 cm^{-1} and 1550 cm^{-1} with increasing nitrogen content in the diamond coating. The cryofractures shown in Fig. 64 are produced after the diamond deposition. It can be seen, that the CrN interlayer has a coating thickness of 2.4 µm. Even on specimen *UVAM 6.5 26* the CrN coating is very homogenous. The diamond coating delaminates by producing the cryofracture. Just at the boarder of the coated area on the polished substrate Fig. 64 b) the diamond coating remained.

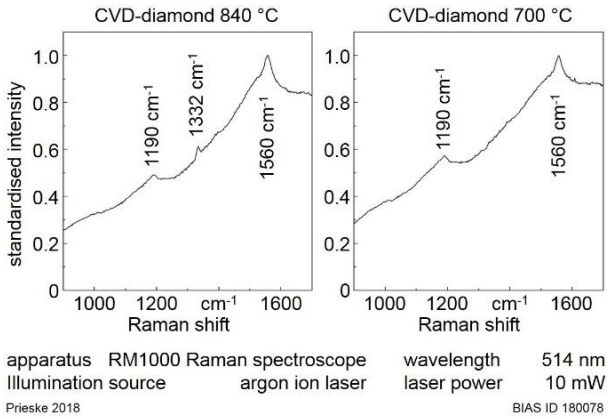

Fig. 63: Raman spectra of the diamond coating deposited at 840 °C (left) and at 700 °C (right).

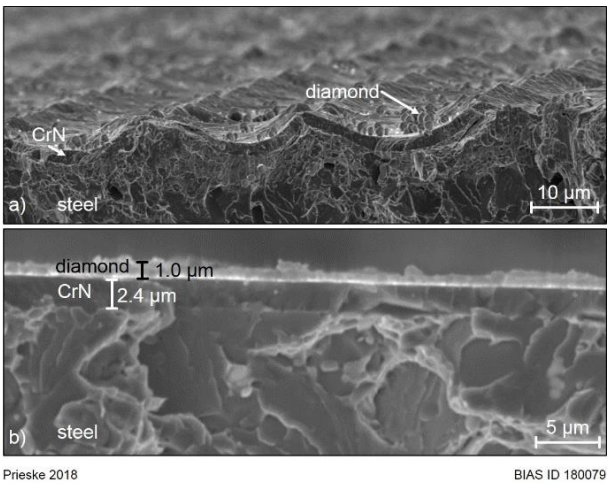

Fig. 64: a) Cryofracture of UVAM 6.5 26 specimen diamond coated at 840 °C and b) cryofracture of the polished specimen after diamond coating at 700 °C.

Hardness measurements in Fig. 65 show that the steel is in a soft annealed state after the deposition process, with a hardness of approximately 220 HV0.1.

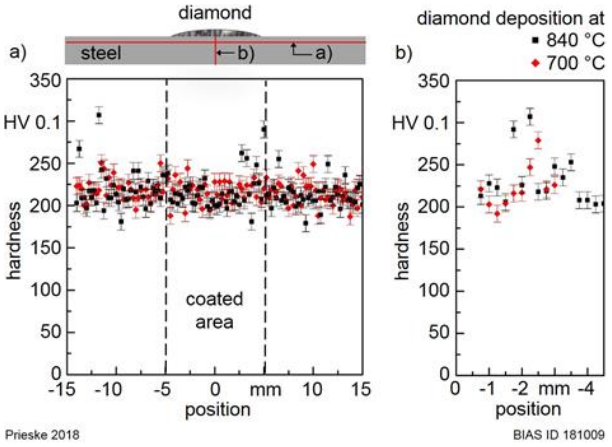

Fig. 65: Hardness measurements of the steel substrate a) parallel and b) perpendicular to the surface after the deposition process at 700 °C and 840 °C.

4 Discussion

The tribological behavior of different diamond and diamond like coatings against the aluminum alloy EN AW-5083-H111 (AlMg4.5Mn0.7) was tested. As reference, also an uncoated and polished steel X153CrMoV12-1 plate was tested and analyzed. The observed high wear rate at the steel plate ($6 \cdot 10^{-6}$ mm^3/Nm) and the round-ended pin ($5 \cdot 10^{-5}$ mm^3/Nm) are explained by excessive abrasive and adhesive wear, also leading to the high COF of about 0.62. Pronounced and dispersed adhesion of aluminum and iron were detected by SEM/EDX on both, the test plate and at the aluminum pin. These results are in good agreement with [45]. Due to the cold welding of aluminum, it can be assumed that the real abrasion of the steel sample is even higher than the calculated wear rate. The COF curve stagnated at a constant value with pronounced curve noises which may be explained by parallel mechanisms. The contact area increases due to abrasion resulting in a decreasing contact pressure. This provides more reaction area for adhesion. The constant COF and the high curve noises may be the result of a mutual build-up and degradation of adhesion layers with simultaneous abrasion on both sides due to alternating sliding motion. After the test, large amounts of steel and aluminum particles were found besides the wear tracks.

The tribological behavior of the tested a-C:H:W/a-C:H-coating system can be separated into several mechanisms and stages. The presence of hydrogen in the a-C:H top layer reduces the density of C-C and C=C bonds in the a-C:H network leading to relatively low hardness of about 1,900 HV0.01 compared to the CVDD coatings with a hardness of about 11500 HV1. The a-C:H:W/a-C:H-coating system exhibits a running-in behavior within the first minutes which is related to the formation of a lubricious graphite-like transfer film after short time [46]. Since carbon residues were detected on the counter aluminum material by EDX, a formation of a tribological transfer film is assumed, resulting in the observed drop of the COF from 0.27 to a nearly constant level of 0.17 after about 1.5 hours. After another 24,000 cycles (1.5 h) the COF curve shows a further decrease to 0.12. The drop in COF can be explained by the abrasive wear and continuous volume loss of the a-C:H top layer due the provision of transfer film. This could explain the drop and subsequent decrease in COF over time, because the intermediate layer contains tungsten and is deposited with graded ramps of bias-voltage and an acetylene flow rate [47]. The presence of tungsten during dry testing seems to have a beneficial effect with respect to the low dry COF. Other works have confirmed that COF further decreases by the formation of WO_3 as soon as a tungsten rich DLC layer is exposed when testing against aluminum (319 al) [46]. WO_3 can provide a lubricious effect since its structure is epitaxial [48]. This could be an indication that small amounts of tungsten incorporated in the hydrogenated carbon matrix are beneficial regarding dry sliding against aluminum. Also amounts of tungsten were found at the counter material after testing indicating the participation of the transfer film formation.

The curve of the as-deposited CVDD-coating is characterized by a constant decrease of COF from 0.42 to 0.36. The curve noises are lower than the resulting noise by sliding against the steel reference. Due to the high hardness of more than 10,000 HV1 and the high surface roughness of Sa 1.19 µm significant abrasion takes place at the round-ended aluminum pin. This is confirmed by the highest wear rate of $6 \cdot 10^{-3}$ mm^3/Nm. Large quantities of aluminum wear debris have accumulated in the roughness valleys. With respect to the CVDD-coating even a material gain was determined which is expressed by a negative value of the wear rate. The remaining aluminum in the wear track on the CVDD-coating interlocks in the valleys of the polycrystalline

surface. The different COF between CVDD and pCVDD can be explained by the strong discrepancy in roughness between Sa 1.19 µm and Sa 0.01 µm. Thereby the loose debris accumulates in the valleys rather than being displaced out of the wear track.

The pCVDD-coating shows an excellent performance in dry sliding against an round-ended aluminum pin with a very constant COF of 0.12 over 10^5 cycles, the lowest wear rate of the round-ended aluminum pin of $4 \cdot 10^{-9}$ mm³/Nm and of the coating of $1 \cdot 10^{-8}$ mm³/Nm. Inside the wear track, wear grooves in the sliding direction of the round-ended aluminum pin have formed as shown in the measured profile of the AFM image in Fig. 31. The depth of the wear grooves is lower than 100 nm. It could be shown, that for polished polycrystalline CVD diamond coatings no formation of nanoripples in transverse direction within a longitudinal wear scar can be detected, as occurs for nanocrystalline diamond coatings [28]. The good performance of the pCVDD-coating is attributed to the interaction of different influencing factors. Firstly, the hardness of the diamond coating of 11525 HV1 gives a lower probability of coating wear under dry sliding contact. Another important factor is the chemically inertness of diamond towards aluminum, as shown by Chattopadhyay et al. [49]. The detected increase of the G peak in the Raman spectrum in result of the tribometer test, determines the slight rise of the graphitic amount. In combination with the detected film on the round-ended aluminum pin after the test, the formation of a transfer film according to Scharf et al. [50] is concluded. The electrical resistance of the round-ended pin rises from a few Ω to more than 60 MΩ due to the formation of the detected film on the round-ended aluminum pin. Tröber et al. [51] showed that thermoelectric currents exert a strong influence on adhesive wear. The occurrence of thermoelectric currents is prevented in the ball-on-plate test through the insulating properties of diamond, which has an electrical resistance of higher than 10^{10} Ω [29], in combination with the high electrical resistance of the formed transfer film.

Regarding the CVD diamond coatings with in-situ evaporated silicon carbide precursors, the peak at 1332 cm^{-1} in the Raman spectra could be detected all over the diamond coating, which proves the existence of a diamond structure [52]. Hence, the evaporated content of silicon carbide does not interfere in such a way that diamond crystal growth is suppressed. On measuring the luminescence spectrum of the diamond layer with incorporated silicon, a peak at 738 nm can be detected. Tóth et al. reported that SiV centers in diamond have an intense zero phonon line at 738 nm [53], which verifies that doping of the diamond coating by silicon is successfully realized in the executed researches. By 2-point resistance measurements a change in the electrical resistance by silicon incorporation could be verified. The application of a 4-point probe van der Pauw resistivity measurement on a single CVD-diamond crystal in the center of the coating leads to a sheet resistance ρ of 2.53 MΩ ± 1.29 MΩ. The pure CVD diamond layer is not machinable by EDM. The successful EDM at silicon doped CVD diamond coatings confirms the change of conductivity characteristics.

CVD-diamond deposition of steel provides several challenges. To enable the coatability of steel by a diamond layer a diffusion barrier is necessary, which prevents the diffusion of carbon into the steel specimen and the diffusion of iron into the diamond coating. The investigations show, that the used HIPIMS chromium nitride coating with a thickness of 2.4 µm successfully worked as a diffusion barrier and has a high adhesion to the steel substrate. In all cases the delamination took place at the interface between CrN interlayer and diamond coating. The used tool steel X153CrMoV12-1 has a thermal linear expansion coefficient of $13.0 \cdot 10^{-6}$ m/(m·K) in the temperature range from 20 °C to 400 °C [54]. Diamond has a thermal expansion coefficient between $1.0 \cdot 10^{-6}$ m/(m·K) and $4.5 \cdot 10^{-6}$ m/(m·K) [55]. This leads to a big mismatch of thermal expansion coefficients and induces large residual stresses. The delamination can be influenced by the surface microstructure. The diamond coating deposited at 840 °C with a coating thickness of 8 µm shows larger delamination than the coating deposited at 700 °C with a thickness of 2 µm. Fig. 56 shows that the prolongation of the steel specimen is less for a deposition at 840 °C with 0.86% than for 700 °C with 0.93%, which is due to the austenite to ferrite transformation. Uncoated areas in the 2 µm thick diamond coatings prevent the generation of high stresses. A higher coating thickness of the diamond coating as well as a closed coated area leads to an increase of the residual stresses. Hardness measurements of the steel after the deposition processes showed that the steel is in annealed condition. The cooling rate from deposition temperature to room temperature in two minutes would be fast enough for a hardening of the steel sample. That leads to the assumption that the total length change could be lower with a higher deposition temperature than 840 °C due to the austenite to ferrite transformation in the steel substrate which results in a volume expansion during cooling in case of a hardening process.

Fig. 57 shows, that the coating adhesion is increased with increasing arithmetic mean height (Sa) to a certain extent. This agrees with the literature cited in the introduction [1, 2, 3, 4, 5]. Regarding the coating thickness

of 8 µm higher roughness values result in a flake-like delamination, with remaining areas of the diamond coating. Whereas low roughness values lead to a delamination of the diamond coating as a foil. The overlap area of *UVAM 6.5 26* reduces the surface roughness, Fig. 30. At the positions of the overlap areas a complete delamination takes place, whereas inside the milling path just local delamination is detected (Fig. 57). Furthermore, the *UVAM 6.5 26* substrate shows that sharp peaks lead to the formation of large diamond crystals (Fig. 59). At the same time the valleys are not coated by a closed diamond layer. This can be explained by a local build-up temperature on the sharp peaks, which results in a local higher diamond growth rate. The diamond coating growth in microwave plasma CVD processes also strongly interacts with mountains, which leads to a reduced diamond growth rate in valleys. To achieve a homogenous coating the chamber pressure is increased, which is not possible in the atmospheric LaPlas CVD process. It is assumed that the higher the peak to valley height is, the higher is the probability that the carbon atoms bind to the larger diamond on the peak rather than to the small diamond crystals in the valley. In Fig. 60 it can be seen that very high Sa and Sdr values, as achieved by corundum blasting, results in an inhomogeneous diamond coating which varies between nano- and microcrystalline diamond. The size of the delaminated areas on the corundum blasted substrates decrease from around 20 µm at 840 °C to 5 µm at 700 °C (compare Fig. 60 and Fig. 62). Interestingly, the ground specimen showed quite good results at a deposition temperature of 700 °C. There are small delaminated areas of maximum 10 µm diameter of the closed diamond coating, but it did not lead to a complete delamination of the coating, even though it has the second smallest roughness values of the investigated microstructures. The delamination always takes place in accordance to the structure. The delaminated area of the diamond coating has the form of stripes on ground substrates, of a foil on polished substrates and is random shaped on the stochastic structures of blasted substrates.

5 Conclusion

With respect to the performed dry tribological tests of specially designed different carbon coatings for their suitability in terms of enabling dry forming of the aluminium alloy EN AW-5083 and subsequent analyses, the following conclusions could be derived: Uncoated and polished steel X153CrMoV12-1 shows high abrasive and adhesive wear by dry sliding against a round-ended aluminium pin and results in a high COF of 0.62. That means that a surface coating is mandatory for forming tools out of that type of steel to realise dry forming of the aluminium alloy EN AW-5083-H111. Rough (Sa 1.19 µm) and hard CVDD-coatings lead to high abrasive wear of the round-ended aluminium pin and are therefore inappropriate for dry aluminium forming. The a-C:H-coating as well as the pCVDD-coating exhibit a short running-in behaviour. The lower hardness of the a-C:H-coating leads to a higher wear rate compared to the pCVDD-coating. The pCVDD-coating shows a very constant dry COF of 0.12 over the complete test duration and negligible wear rates.

UVAM can be used to generate defined and reproducible microstructures in steel substrates that can be simulated by a surface prediction tool and varied - in technological limits - in their geometrical properties. It could be shown that the surface microstructure has a high impact on the interlocking between coating and surface. Low surface roughness values up to 0.9 µm lead in case of 8 µm thick diamond coatings to a delamination of the diamond coating in form of a diamond foil. Higher roughness values result in a flake-like delamination, with remaining areas of the diamond coating. None of the microstructures investigated in this study was able to overcome the residual stress induced by thermal expansion of the steel substrate in such a way, that it prevents delamination of the coating entirely. The following conclusions of expedient parameters can be drawn to achieve a closed diamond coating on steel:

- Before the diamond deposition of a steel specimen, the thermal expansion of the specific type of steel needs to be investigated. By considering that the austenite to ferrite transformation has a strong influence on the prolongation of the steel, the most advantageous deposition temperature and cooling rate needs to be estimated.
- For the diamond deposition on the steel X153CrMoV12-1 the deposition temperature needs to be either lower than 650 °C where the length change of the steel specimen is 0.85% or higher than 840 °C with a hardening of the steel and an accompanied reduction of the thermal expansion.
- Sharp peaks at the microstructured specimen surface should be avoided due to local build-up temperature, which leads to an inhomogeneous diamond coating thickness. Furthermore, a certain roughness higher than Sa 0.1 µm supports the adhesion. The UVAM process for the production of modifiable, deterministic microstructures on surfaces to be coated appears to be suitable against this background.

For the overall vision of dry metal forming it could be shown that the advantage of the a-C:H-coating is the deposition process, which enables a large area deposition as well as a good adhesion strength on various different substrate materials. The CVD-diamond deposition process still has research demands regarding the adhesion strength on steel substrates and the large area deposition. The need of a subsequent polishing process provides the opportunity to adjust a different roughness at different positions of the forming tool to control the material flow. Focusing on the performance of the different coatings in the dry tribological ball-on-plate test, the pCVDD coating is the most promising of the tested carbon coatings to enable dry aluminium forming with a long lifetime of the coated tool. By in situ silicon carbide sublimation, a possibility has been demonstrated for atmospheric CVD processes to reduce the electrical resistance of CVD diamond layers without the use of toxic gases. The electrical resistance of the coating could be reduced with a silicon doping concentration in the order of 10^{20} cm^{-3} in range between 10^4 Ω and 10^6 Ω. Electrical discharge machining of CVD diamond coatings has been made possible by silicon doping, which means that the resistivity has been reduced to below 100 Ω·cm.

Acknowledgements

The authors would like to thank the German Research Foundation (DFG Deutsche Forschungsgemeinschaft) for funding this work under the project number 244972655.

References

[1] M. Amaral, F. Almeida, A. J. S Fernandes, F. M. Costa, F. J. Oliveira, R. F. Silva: The role of surface activation prior to seeding on CVD diamond adhesion. Surf. Coat. Technol. 204 21–22 (2010) 3585–3591
[2] R.K. Singh, D.R. Gilbert, J. Fitz-Gerald, S. Harkness, D.G. Lee: Engineered interfaces for adherent diamond coatings on large thermal-expansion coefficient mismatched substrates. Science 272 (1996) 396–398
[3] H. Wako, T. Abe, T. Takagi, T. Ikohagi: Comparison of diamond film adhesion on molybdenum substrates with different surface morphologies. Appl. Surf. Sci. 256 5 (2009) 1466–1471
[4] Z. Xu, L. Lev, M. Lukitsch, A. Kumar: Effects of surface pretreatments on the deposition of adherent diamond coatings on cemented tungsten carbide substrates. Diamond and Related Materials 16 3 (2007) 461–466
[5] H. Gomez, D. Durham, X. Xiao, M. Lukitsch, P. Lu, K. Chou, A. Sachdev, A. Kumar: Adhesion analysis and dry machining performance of CVD diamond coatings deposited on surface modified WC–Co turning inserts. J. Mater. Process. Technol. 212 2 (2012) 523–533
[6] D.G. Lee, D.R. Gilbert, S.M. Lee, R.K. Singh. Surface composites: a novel method to fabricate adherent interfaces in thermal-mismatched systems. Composites Part B: Engineering 1999, 30, pp. 667–674.
[7] T. Grögler, E. Zeiler, A. Hörner, S.M. Rosiwal, R.F. Singer. Microwave-plasma-CVD of diamond coatings onto titanium and titanium alloys. Surface and Coatings Technology 1998, 98, pp. 1079–1091.
[8] T. Grögler, A. Franz, D. Klaffke, S.M. Rosiwal, R.F. Singer. Tribological optimization of CVD diamond coated Ti-6Al-4V1. Diamond and Related Materials 1998, 7, pp. 1342–1347.
[9] T. Grögler, O. Plewa, S.M. Rosiwal, R.F. Singer. CVD diamond films as protective coatings on titanium alloys. International Journal of Refractory Metals and Hard Materials 1998, 16, pp. 217–222.
[10] E. Zeiler, D. Klaffke, K. Hiltner, T. Grögler, S.M. Rosiwal, R. F. Singer. Tribological performance of mechanically lapped chemical vapor deposited diamond coatings. Surface and Coatings Technology 1999, 116–119, pp. 599–608
[11] P.Y. Lim, F.Y. Lin, H.C. Shih, V.G. Ralchenko, V.P. Varnin, Y.V. Pleskov, S.F. Hsu, S.S. Chou, P.L. Hsu. Improved stability of titanium based boron-doped chemical vapor deposited diamond thin-film electrode by modifying titanium substrate surface. Thin Solid Films 2008, 516, pp. 6125–6132
[12] M. Prieske, C. Wiegmann, M. Schwander, F. Vollertsen: Feedback control of the substrate surface temperature in a laser-induced plasma CVD process. Dry Met. Form. OAJ FMT 1 (2015) 1-4
[13] M.G. Peters, R.H. Cummings: Methods for coating adherent diamond films on cemented tungsten carbide substrates. Patent US5236740A, 17 August 1993.
[14] J.G. Buijnsters, P. Shankar, W. Fleischer, W. van Enckevort, J.J. Schermer, J.J. Ter Meulen: CVD diamond deposition on steel using arc-plated chromium ni-tride interlayers. Diamond and Related Materials 11, 3-6 (2002) 536–544
[15] O. Glozman, A. Hoffman: Adhesion improvement of diamond films on steel substrates using chromium nitride interlayers. Diamond and Related Materials 6 (1997) 796–801
[16] A.C. Ferrari, J. Robertson: Raman spectroscopy of amorphous, nanostructured, diamond–like carbon, and nanodiamond. Mathematical, Physical and Engineering Sciences 362 (2004) 2477–2512
[17] L.J. van der Pauw: A method of measuring specific resistivity and Hall effect of discs of arbitrary shape. Philips Research Reports 13 (1958) 1–9
[18] DIN EN ISO 1071-12 Deutsche Norm - Hochleistungskeramik - Verfahren zur Prüfung keramischer Schichten - Teil 12: Schwingungs-Verschleißprüfung (2010)
[19] M. Pereira, W. Yan, B.F. Rolfe: Modeling of Contact Pressure in Sheet Metal Forming. Materials Science Forum 561-565 (2007) 1975-1978
[20] DIN EN ISO 14577-1 Deutsche Norm – Metallische Werkstoffe – Instrumentierte Eindringprüfung zur Bestimmung der Härte und anderer Werkstoffparameter (2012)
[21] P. Scholz, R. Müller, R. Börner, R. Kühn, A. Schubert: Dry forming of aluminium sheet metal: Influence of different types of forming tool microstructures on the coefficient of friction. 18th Int. ESAFORM Conf. Mater. Form. (ESAFORM 2015), April 15-17, 2015, Graz, Austria. Key Engineering Materials Vol. 651-653 (2015), 480-485
[22] D. Tabor: Junction Growth in Metallic Friction: The Role of Combined Stresses and Surface Contamination. Proceedings of the Royal Society A 251 (1959) 378-393
[23] M.C. Shaw, A. Ber, P.A. Mamin: Friction Characteristics of Sliding Surfaces Undergoing Subsurface Plastic Flow. J. Basic Eng. 82 (1960) 342-345
[24] F. Bowden, D. Tabor, E.H. Freitag: Reibung und Schmierung fester Körper. Springer-Verlag, Berlin (1959)
[25] D.K. Leu: A simple dry friction model for metal forming process. Journal of Materials Processing Technology 209 (2009) 2361-2368
[26] R. Börner, P. Scholz, R. Kühn, A. Schubert, H. Zeidler, R. Müller: Micro structuring of coated tools for dry sheet metal forming of Aluminium alloys. euspen's 15th International Conference & Exhibition, Leuven, Belgium (2015)

[27] J. Asmussen, D. Reinhard (Hrsg.): Diamond films handbook. CRC Press New York NY (2002) S. 340 ff.
[28] V. Podgursky, T. Hantschel, A. Bogatov, E. Kimmari, M. Antonov, M. Viljus, V. Mikli, M. Tsigkourakos, W. Vandervorst, J.G. Buijnsters, A.T. Raadik, P. Kulu: Rippling on wear scar surfaces of nanocrystalline diamond films after reciprocating sliding against ceramic balls. Tribol. Lett. 55 (2014) 493-501
[29] M. Tsigkourakos, T. Hantschel, D.K. Simon, T. Nuytten, A.S. Verhulst, B. Douhard, W. Vandervorst: On the local conductivity of individual diamond seeds and their impact on the interfacial resistance of boron-doped diamond films. Carbon 79 (2014) 103-112
[30] A.T. Collins, M. Kamo, Y. Sato: A spectroscopic study of optical centers in diamond grown by microwave-assisted chemical vapor deposition. Journal of Materials Research 5 (1990) 11, S. 2507–2514
[31] M. Iwai, A. Sharma, W.L. Pan, S. Sano, T. Uematsu, K. Suzuki, EDM Properties of a Low Wear Electrically Conductive CVD Diamond Electrode. In: Key Engineering Materials 339 (2007), pp. 168- 176. 2003.
[32] M.A. Haikal Ahmad, M. Zulafif Rahim, M.F. Mohd Fauzi, N. Hafizah Azis, A.E. Ismail, M. Fahrul Hassan, A.M.T. Arifin, M.S. Yusof, M. Rasidi Ibrahim: Electrical Discharge Machining of Polycristalline Diamond Using Copper Electrode – Finish Condition. In. Proc. of IOP Conference on Materials Science and Engineering, 203 (2017)
[33] Z.N. Guo, Z. G. Huang, C. Y. Wang: Smoothing CVD diamond films by wire EDM with high traveling speed. In: Key Engeneering Materials, 257-258, 489-494
[34] W.Z. Lu, D.W. Zu, M. Wang, F. Xu, X.F. Li: Study on EDM polishing of CVD diamond films. In: Z.J. Yuan, X.P. Xu, D.W. Zuo, J.L. Yuan, Y.X. Yao (Eds.), Advances in machining and manufacturing technology. Zurich-Uetikon: Trans Tech Publications Ltd.
[35] R.H. Olsen, R.C. Dewes, D.K. Aspinwall: Electrical Discharge Machining of conductive CVD Diamond tool blanks. In: Journal of Materials Processing Technology, 149, 627-632, 2004.
[36] R. Börner, T. Junge, A. Schubert: Oberflächensimulation und experimentelle Untersuchungen zur Mik-rostrukturierung von Stahlwerkstoffen mittels schwingungsüberlager-tem Planfräsen im Ultraschallbereich. Dry Met. Form. OAJ FMT 1 (2017) 017-024
[37] R. Börner, S. Winkler, T. Junge, C. Titsch, A. Schubert, W.-G. Drossel: Generation of functional surfaces by using a simulation tool for surface prediction and micro structuring of cold-working steel with ultrasonic vibration assisted face milling. Journal of Materials Processing Technology 2018, 255, pp. 749–759.
[38] M. Prieske, R. Börner, A. Schubert. Influence of the surface microstructure on the adhesion of a CVD-diamond coating on steel with a CrN interlayer. MATEC Web of Conferences 2018, 190, pp. 14008
[39] B. Lauwers, F. Klocke, A. Klink, A.E. Tekkaya, R. Neugebauer, D. Mcintosh: Hybrid processes in manufacturing. CIRP Annals - Manufacturing Technology 63, 561–583.2014
[40] A. Maurotto, C.T. Wickramarachchi: Experimental investigations on effects of frequency in ultrasonically-assisted end-milling of AISI 316L: A feasibility study. Ultrasonics 65, 113–120. 2016
[41] M. Kuruc, M. Zvončan, J. Peterka: Investigation of Ultrasonic Assisted Milling of Aluminum Alloy AlMg4.5Mn. Procedia Engineering 69, 1048–1053. 2014
[42] J.G. Buijnsters, P. Shankar, J.J. Ter Meulen: Direct deposition of polycrystalline diamond onto steel substrates. Surface and Coatings Technology 201, 22-23 (2007) 8955–8960
[43] A.C. Ferrari: Raman spectroscopy of graphene and graphite: disorder, electron–phonon coupling, doping and nonadiabatic effects. Solid State Communications 143 (2007) 47–57
[44] Q. Zhang, S.F. Yoon, J.A. Rusli, Y.-P. Guo: The effects of nitrogen flow on the Raman spectra of polycrystalline diamond films. Microelectronics Journal 29 (1998) 875–879
[45] H. Hasselbruch, M. Herrmann, A. Mehner, B. Kuhfuss, H.-W. Zoch.: Incremental dry forging – Interaction of W-DLC coatings and surface structures for rotary swaging tools. Procedia Manufacturing 8 (2017) 541-548
[46] A. Abou Gharam: Tribological behaviour of H- and W-DLC coatings: Effects of environment and temperature on adhesion. Electronic Theses and Dissertations (2014) University of Windsor, Canada. Paper 5058
[47] H. Hasselbruch, M. Herrmann, A. Mehner, H.-W. Zoch, B. Kuhfuss: Development, characterization and testing of tungsten doped DLC coatings for dry rotary swaging. MATEC Web of Conferences 21, 08012 (2015) 1-8
[48] O.D. Greenwood, S.C. Moulzolf, P.J. Blau, R.J. a Lad: The influence of microstructure on tribological properties of WO3 thin films. Wear 232 (1999) 84-90
[49] A.K. Chattopadhyay, P. Roy, A. Ghosh, S.K. Sarangi: Wettability and machinability study of pure aluminium towards uncoated and coated carbide cutting tool inserts. Surface and Coatings Technology 203 (2009) 941-951
[50] T.W. Scharf, I.L. Singer: Role of the Transfer Film on the friction and wear of metal carbide reinforced amorphous carbon coatings during run-in. Tribol Lett 36 (2009) 43-53
[51] P. Tröber, H.A. Weiss, T. Kopp, R. Golle, W. Volk: On the correlation between thermoelectricity and adhesive tool wear during blanking of aluminium sheets. International Journal of Machine Tools and Manufacture 118/119 (2017) 91-97
[52] A.C. Ferrari, J. Robertson: Interpretation of Raman spectra of disordered and amorphous carbon. Phys. Rev. B, 61 (2000) 14095–14107
[53] S. Tóth, L. Himics, M. Veres, Z. Balogh, V.G. Ralchenko, M. Koós: Zero-phonon line characteristics of SiV center emission in microcrystalline diamond probed with intensive optical excitation. Journal of Luminescence 158 (2015) 260–264
[54] http://www.dorrenberg.es/download/aceros/DOE/1.2379_deu.pdf, opened 19th Jan. 2018
[55] K. Kellermann, C. Bareiß, S.M. Rosiwal, R.F. Singer: Well Adherent Diamond Coatings on Steel Substrates. Advanced Engineering Materials 10, 7 (2008) 657–660